Research papers

An automatic ANN-based procedure for detecting optimal image sequences supporting LS-PIV applications for rivers monitoring

Francesco Alongi [*], Dario Pumo , Carmelo Nasello , Salvatore Nizza , Giuseppe Ciraolo , Leonardo V. Noto

Dipartimento di Ingegneria – Università degli studi di Palermo, Viale delle Scienze, Ed. 8, 90128, Palermo, Italy

ARTICLE INFO

ABSTRACT

River flow monitoring has recently experienced rapid development due to advancements in optical methods, which are non-intrusive and enhance safety conditions for operators. Surface velocity fields are obtained recording and analyzing displacements of floating tracer materials, artificially introduced or already present on the water surface. River discharge can be assessed coupling the surface velocity fields with geometric data of a cross section. The accuracy of optical techniques is strongly affected by different environmental and hydraulic factors, and software parameterization, with tracer features that often play a prominent role. An adequate density and spatial distribution of tracer is required to ensure a complete characterization of surface velocity fields. In practical applications such conditions might occur only for a limited portion of the entire acquired images sequence. This work proposes an automatic procedure for identifying and extracting the best portion of a recorded video in terms of seeding characteristics and demonstrates how LS-PIV software performances can be enhanced through this approach. The procedure is implemented through a data-driven empirical approach based on an Artificial Neural Network, trained using data collected during an extensive measurement campaign across different rivers in Sicily (Italy). Performances are evaluated in terms of error in reproducing surface velocity profiles along specific transects, where benchmark profiles derived using an Acoustic Doppler Current Profiler are available. The procedure, also tested via numerical simulations on synthetic image sequences, outperformed an approach based on an existing metric for seeding characterization and represents a simple and useful tool for LS-PIV based applications.

1. Introduction

River discharge monitoring is typically characterized by considerable uncertainty compared to other hydrological variables like rainfall and temperature. A conventional measurement approach implies the adoption of the velocity-area method based on the evaluation of the mean flow velocity and the wetted cross-sectional area along a transect.

Velocity measurements are traditionally performed with mechanical or electromagnetic current meters (Herschy, 1995), while in the last decades, current meters have been replaced by more technologically advanced instruments, i.e., Acoustic Doppler Current Profilers (ADCPs). Such instruments require direct contact with water flow, sometimes exposing sensors and operators to risks especially under flood conditions. The intrusiveness issue of current meters has been partially addressed by the adoption of ADCPs. However, conventional approaches

are generally time-consuming and expensive, requiring highly specialized personnel (Ioli et al., 2020).

The improvement of discharge measurement techniques is one of the major tasks in hydrometry (Larnier et al., 2021; Riggs et al., 2022). Recent technological advances have given a strong impulse to the development of innovative approaches based on remote sensing methods, such as optical techniques using radars, terrestrial and satellite image detectors (Costa et al., 2006; Pavelsky, 2014; Pearce et al., 2020; Junqueira et al., 2021; Rahman Khan et al., 2021).

This work focuses on image-based techniques, whose large-scale application to field sites represents a new and promising frontier in river monitoring (Tauro et al., 2017; Dal Sasso et al., 2021a) that deserves further investigations aimed at the identification of appropriate operational protocols, still lacking. More specifically, it is here considered the Large-Scale Particle Image Velocimetry (LS-PIV) method.

LS-PIV is one of the most used optical techniques (Fujita et al., 1998; Muste et al., 2008; Le Coz et al., 2014) and it is based on four key phases: (i) seeding and recording; (ii) images pre-processing; (iii) images processing; and (iv) images post-processing.

In the seeding phase, artificial tracer material (e.g., wooden chips, bark) is introduced and dispersed over the liquid surface, when natural tracers (e.g., bubbles, foam, leaves) are not present with adequate consistency. Tracer should be of a clearly distinguishable color, floating on the surface, and with an adequate shape to minimize the impact of wind. The seeding phase represents one of the most complex activities in practical applications, since the accuracy of the subsequent steps strongly depends on tracer particle density and distribution over space and time, which are characteristics that are hard to control during field campaigns. It is worth emphasizing that some applications do not use any forms of natural/artificial tracers, analyzing the water surface ripples caused by wind and hydraulic turbulence (Tauro et al., 2016; Yeh et al., 2019).

During the recording phase, tracer motion is captured by recording devices that can be located on bridges, riverbanks or by Unmanned Aerial Vehicles, UAVs (Detert and Weitbrecht, 2015; Lewis et al., 2018; Pearce et al., 2020; Bandini et al., 2021; Lagogiannis and Dimitriou, 2021; Koutalakis and Zaimes, 2022). Camera acquisitions are frequently affected by disturbing effects such as shake due to wind or vehicular traffic, sudden shifts due to rough movements of the operator, fluctuations caused by the oscillation of drones during flights (Jolley et al., 2021; Liu et al., 2021). Also lens and perspective distortions frequently occur (Le Boursicaud et al., 2016; Lewis and Rhoads, 2018; Li et al., 2019), as well as disturbances due to reflections, glint, and shading (Acharya et al., 2021).

Once frames are extracted from the acquired videos, at the acquisition or at a lower frame-rate, some pre-processing steps may be applied, and they typically include: (i) stabilization for removing undesired movements of cameras, (ii) orthorectification to remove optical and perspective distortions, (iii) graphical enhancement to minimize reflections and improve the contrast between tracer and background.

In the processing phase, a statistical analysis is performed through specific software packages, often freely available and open-source, such as PIVlab (Thielicke and Stamhuis, 2014), FUDAA-LSPIV (Le Coz et al., 2014), KLT-IV (Perks, 2020), and RIVeR (Patalano et al., 2017). Software programs use cross-correlation algorithms to detect the most probable frame-by-frame tracer displacement and derive instantaneous surface velocity fields. These last are then post-processed using filters to discard outlier and incoherent (e.g., scarcely correlated) displacement/velocity vectors, and spatially interpolate missing data. The mean surface velocity field is finally obtained by averaging the instantaneous surface velocity fields.

An additional step can be considered when discharge is required (Creutin et al., 2003; Hauet et al., 2008). In this case, the discharge in a transect is evaluated as the product of the wetted area, derived from knowledge of the cross-section geometry, and the mean flow velocity, that is often computed as a function of the mean surface velocity at the same cross-section, assuming a constant ratio between mean surface velocity and depth-averaged velocity equal to 0.85 (Hauet et al., 2018).

The density and the spatio-temporal distribution of the tracer play a crucial role in boosting the performance of the cross-correlation algorithms. Several efforts have recently been made to study the optimal setup for field campaigns in terms of optimal tracer density, distribution, frame-rate, length of the processed sequence, software parametrization, etc., via numerical experiments (Dal Sasso et al., 2018; Pizarro et al., 2020b; Pumo et al., 2021; Bodart et al., 2022) or analyzing field measurements (Watanabe et al., 2021; Zhao et al., 2021). Nevertheless, seeding conditions are highly influenced by the river hydraulic conditions and the seeding field operations, and achieving and maintaining desired "target" tracer features in practical applications is extremely difficult, especially when the tracer is introduced manually.

According to Pizarro (2020b) errors in evaluating surface velocity fields are directly related to the seeding characteristics, and often the acquired video sequences may be partially or totally not suitable for cross-correlation analyses. Nevertheless, it is sometimes possible to identify, select and process a sub-sequence from the original videos over which the seeding characteristics maintain desirable properties, i. e., adequate and steady-state tracer density over the various frames, with particles having uniform spatial distribution over the entire area of analysis (Pizarro et al., 2020a, 2020b; Dal Sasso et al., 2021a). Pizarro et al. (2020b) introduced a metric, the Seeding Distribution Index (SDI), to characterize the seeding river status in terms of density and distribution. SDI was derived numerically, through the analysis of synthetic sequences generated under controlled seeding conditions and considering different tracer spatial-clustering levels and densities. The authors showed that LS-PIV based analyses of sub-sequences with low SDI were able to provide more accurate velocity estimates than sub-sequences with high SDI, demonstrating the importance of selecting an optimal sub-sequence based on tracer characteristics for the processing phase.

The aim of the present work is to verify what emerged from the numerical approach by Pizarro et al. (2020b), structuring a new automatic procedure on empirical basis capable of identifying and extracting from the entire recorded video the best sub-sequence in terms of tracer features, with the final aim to enhance LS-PIV based estimations. A new metric, named global index (GI), is here introduced for the evaluation of the seeding characteristics over the entire sequence, and it integrates four different indicators related to the density and the spatial and temporal distribution of the tracer; the proposed procedure is able to detect the best sub-sequence that can be extracted from raw recorded videos based on the GI.

The procedure is based on a Multi-Layer Perceptron (MLP) Artificial Neural Network (ANN), developed exploiting measurements arising from a field campaign carried out on different Sicilian rivers, in Italy, and applying one of the most used LS-PIV software, i.e. PIVlab (Thielicke and Stamhuis, 2014). The results are evaluated in terms of errors in reproducing the surface velocity profile along specific transects for each case study, for which a benchmark profile derived by an ADCP is available. The use of the procedure is simple, fast, and suitable for practical applications. Validation in case studies not used for generating the ANN demonstrates how the adoption of such procedure may lead to a reduction of the error in the mean surface velocity reproduction even in the order of the 40 %. The proposed procedure was also successfully tested under controlled conditions, through numerical analyses on synthetic video sequences generated *ad hoc*, demonstrating its suitability also under conditions different from those characterizing the field case studies here considered.

The paper is organized as follows: Section 2 presents case studies and the experimental set-up considered for each case. The field protocol adopted for the application of both LS-PIV and ADCP techniques is described in the same section, together with the procedure adopted to obtain the benchmark velocity profiles. Section 2 also describes the proposed automatic procedure, while results and discussion are reported in Section 3 and 4, respectively. Conclusions are provided in the final section.

2. Methodology

2.1. Case studies

Data arising from an extensive field campaign in Sicily were analyzed to develop the proposed procedure. Topographic surveys and simultaneous flow river measurements by LS-PIV technique and ADCP along specific transects were performed in six rivers, depicted in Fig. 1. A total of twelve independent field measurements were acquired on different days during the period 2020–2021 (Table 1): single measurements were performed in the Palma and Imera rivers (i.e., PA-01, and IM-01) and at two different sections of the Belice river, i.e., in the upstream Ponte Belice section (BEP-01) and in the downstream Marinella section (BEM-
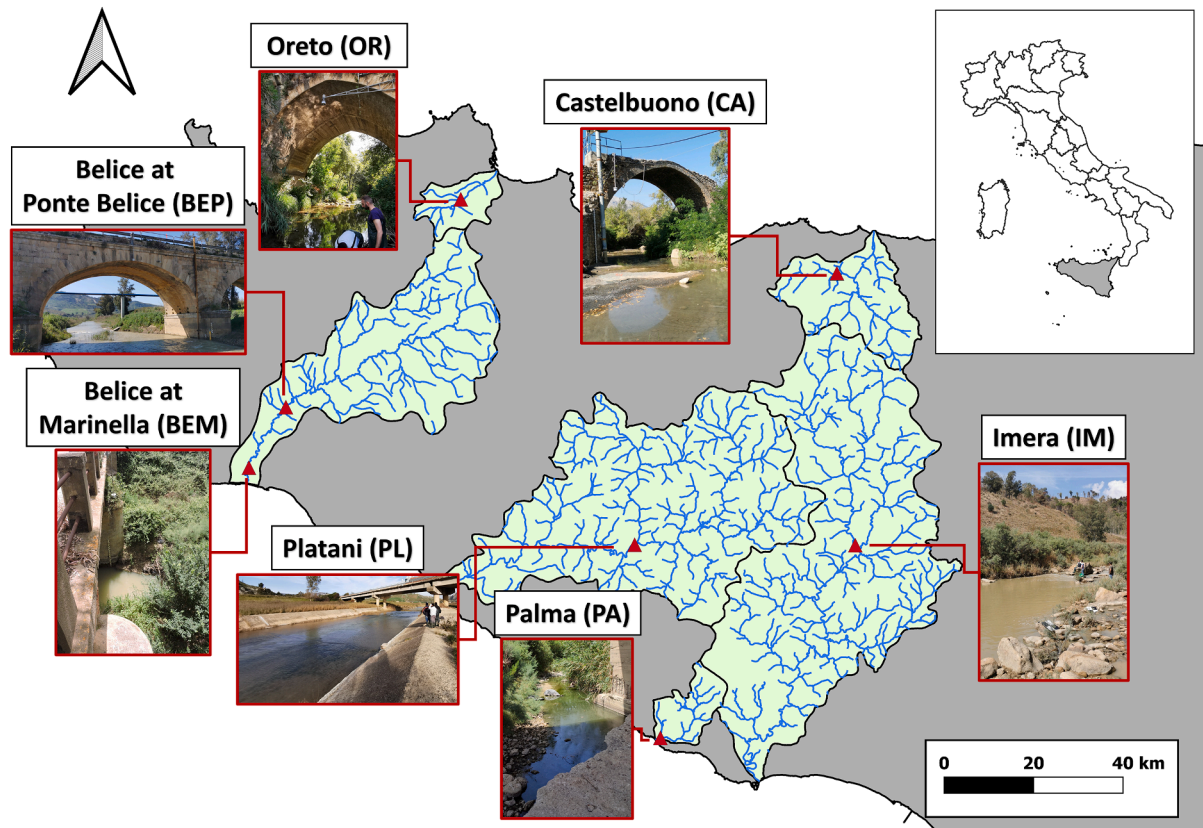
Fig. 1. Monitored rivers and correspondent drainage areas. Triangular markers represent the measurement locations.

Table 1
Identification code (IDm) associated to each measurement, time of acquisition (Date), drainage areas (Ar), channel features (Type, Geometry, and prevalent Riverbed material), cross-sectional width (Wd), and acquisition modality (Acq) at the various case studies.

IDm	Date	Ar [km²]	Channel				Acq
			Type	Geometry	Riverbed	Wd [m]	
OR-01	07/02/20	70.8	natural	irregular	sandy	5	bridge
OR-02	14/09/20	70.8	natural	irregular	sandy	5	bridge
OR-03	04/06/21	70.8	natural	irregular	sandy	5	bridge
PL-01	18/06/20	1221	artificial	regular	concrete	4.5	drone
PL-02	08/09/20	1221	artificial	regular	concrete	4.5	drone
PL-03	07/05/21	1221	artificial	regular	concrete	4.5	drone
CA-01	09/04/21	938	natural	regular	rocky	6	bridge
CA-02	23/11/21	938	natural	regular	rocky	6	bridge
BEP-01	18/10/21	858	artificial	regular	concrete	2.5	drone
BEM-01	18/10/21	938	natural	irregular	sandy	4.5	bridge
PA-01	07/05/21	119	natural	irregular	pebbly	5.5	bridge
IM-01	15/09/20	634	natural	irregular	pebbly	15	drone

01), while multiple measurements over time were performed in the Oreto (OR-01, OR-02 and OR-03), Platani (PL-01, PL-02 and PL-03), and Castelbuono (CA-01 and CA-02) rivers.

Case studies are representative of different river characteristics, environmental and hydraulic conditions, as well as different modalities of video sequences acquisition (Tables 1 and 2). In particular, Table 1 provides a comprehensive overview of the case studies at measurement sections, reporting information concerning the drainage area (Ar) and some specific characteristics of the river channel derived from direct observation, i.e., the anthropization level (natural or artificial), the overall shape (regular or irregular), the type of prevalent material of the riverbed, and the channel width. Table 1 also reports devices used for video recording at each case. Different operative setups for the application of LS-PIV technique were applied; while in OR, CA, BEM and PA cases video sequences were acquired by a camera mounted on a tripod in fixed position on a bridge, in the remaining sections (i.e., PL, BEP and IM) video acquisition was performed from a drone. As in most of the Sicilian rivers, the flow regime for the selected case studies is ephemeral and intermittent (Pumo et al., 2013, 2014).

A total of 10 measurements (i.e., OR-01, OR-02, OR-03, PL-01, PL-02, PL-03, CA-01, CA-02, BEP-01, and IM-01) were used during the structuring and the calibration phase of the procedure, whilst the remaining two case studies (i.e., BEM-01 and PA-01) were used exclusively for validation purposes.

2.2 ADCP measurements

2.2.1. StreamPro ADCP, WinRiverII, and operational field protocol

Benchmark surface velocity profiles at specific transects were derived for each field measurement using an ADCP, which measures

Table 2

Discharge (Q), cross-section wetted area (A), and mean velocity (V) estimated by the ADCP for all the case studies. Total number of valid transect-measurements (N_v) out of the total number of performed transect-measurements (N_p), total exposure time (t_{ex}), maximum relative residual ($\max|RRi|$) of the valid transect-measurements and corresponding Maximum Permissible Relative Residual (MPRR).

ID_m	Q $[m^3/s]$	A $[m^2]$	V $[m/s]$	$N_v(N_p)$ [-]	t_{ex} [min]	max|RRi| [%]	MPRR [%]
OR-01	0.298	3.77	0.079	7 (10)	59	2.3	8.6
OR-02	0.164	3.24	0.050	6 (8)	27	5.5	7.5
OR-03	0.223	2.87	0.077	5 (8)	46	2.9	6.3
PL-01	0.233	1.59	0.146	6 (8)	15	6.7	7.5
PL-02	0.316	1.63	0.193	11 (12)	12	7.1	12.6
PL-03	0.630	3.09	0.203	4 (6)	13	1.9	5
CA-01	0.272	2.62	0.103	5 (6)	34	4.7	6.3
CA-02	0.392	2.87	0.136	4 (6)	63	1.9	5
BEP-01	0.180	2.40	0.075	4 (6)	12	2.3	5
BEM-01	0.654	3.71	0.176	8 (8)	19	4.1	9.7
PA-01	0.050	1.51	0.033	5 (6)	34	5.2	6.3
IM-01	0.382	10.05	0.038	4 (10)	32	4.9	5

water velocity using Doppler's principle (Muste et al., 2004). More specifically, the StreamPro ADCP, produced by Teledyne Marine RD Instruments, was used to measure velocity and bathymetry through WinRiver II (v2.22) software. Two profiling modes (WM12 and WM13), available in WinRiver II, were used depending on the hydraulic conditions and the depth of the river under analysis.

A standard operational field protocol according to the United States Geological Survey guidelines (Mueller et al., 2009) and the World Meteorological Organization standard (World Meteorological Organization, 2008) was adopted for ADCP discharge measurements, accounting for the following requirements:

i. perform multiple reciprocals measurements along a transect to minimize directional bias;
ii. exposure time (i.e., total duration of the measurements) longer than 720 s to average any possible disturbance effects over time;
iii. removal of outlier measurements, characterized by an excessive deviation in the discharge from the mean over all the measures.

Regarding the last point, WinRiver II software provides a "Discharge Summary", which uses a Dynamic Residual Analysis algorithm allowing for a fast deviation evaluation. The relative residual of a discharge transect-measurement (RR_i) is computed as:

$$RR_i = \frac{Q_i - Q_{mean}}{Q_{mean}} [\%] \tag{1}$$

where Q_i is the generic i-th discharge transect-measurement, and Q_{mean} is the mean value over all the acquired discharge transect-measurements. The residual control criterion is:

$$|RR_i|\langle MPRR \tag{2}$$

where *MPRR* is the Maximum Permissible Relative Residual, whose value depends on the number of performed transect-measurements: the greater the number of measures, the greater the *MPRR* value. In WinRiver II, *MPRR* ranges from 5 % with 4 transect-measurements up to almost 20 % with 20 transect-measurements. Following this approach, transect-measurements with relative residual over the *MPRR* were discarded, deriving final assessed value of ADCP at each measurement as averaged values over the retained transect-measurements (Table 2).

2.2.2. ADCP based benchmark surface velocity profile

ADCP instrument cannot measure surface velocities due to transducer submersion. To infer benchmark surface velocity profile from each ADCP measurement, the approach proposed by Le Coz et al. (2010) and

Pearce et al. (2020) was adopted. During a transect-measurement, ADCP collects raw velocity data at different depths along several verticals, dividing the water columns into a finite number of cells. Thus, from each retained transect-measurement by ADCP, it is possible to build a dataset containing paired normalized velocity-depth data at each vertical, with velocities normalized with respect to the mean velocity along the vertical, and depths normalized with respect to the total depth for the corresponding vertical. For each field campaign, a unique dataset can be obtained by aggregating all the normalized datasets from each retained transect-measurement.

The normalized depth (Z_{norm}), ranging from zero (bottom) to one (surface), is binned into 0.05-wide intervals, evaluating the median of the normalized velocities within each bin. All the assessed median velocities at each bin are paired with the average normalized depth of the corresponding bin, and the obtained points are interpolated by a power law:

$$V_{norm}(Z_{norm}) = aZ_{norm}^n \tag{3}$$

where $V_{norm}(Z_{norm})$ is the normalized flow velocity at the normalized depth Z_{norm}, while a and n are the power law parameters. For example, Fig. 2a shows the cloud of paired normalized velocity-depth points and the derived power law curve in a case study randomly selected (PL-03).

The exponent n is often fixed equal to 1/6 (Muste et al., 2008; Le Coz et al., 2010, 2012); in this work, site-specific values for both a and n were assessed. The coefficient a represents the normalized surface velocity at the water surface ($Z_{norm} = 1$). Thus, once a and n are computed, the surface velocity for a generic vertical can be obtained multiplying a-coefficient by the normalization term, i.e., the mean velocity along that vertical. A point cloud of surface velocities is then obtained applying the described procedure to all the verticals of a field campaign dataset (Fig. 2b). The final surface velocity profile was obtained again by a binning procedure, dividing the total length of the transect into equal size bins (i.e., 0.3 m), and associating to each bin the mean of surface velocities falling in that bin. Finally, a bootstrap resampling approach was used to derive the 95 % confidence intervals for the surface velocity profile obtained at the various field campaigns (Fig. 2b).

2.3. LS-PIV measurements

2.3.1. Instruments and experimental set-up

The equipment used to carry out LS-PIV measurements includes tracer materials and devices for video recording and topographic survey. Artificial tracer released manually from the riverbanks was used for all the measurements, exploiting a commercially available and low-cost wooden materials, i.e., chips and conifer bark with variable shape and size (prevalently cylindrical shaped, with maximum linear dimension between 25 and 40 mm). The selected material is scarcely sensitive to wind disturbances and provides a good contrast with the background.

Images were recorded using a commercial camera and a small drone. In the first case, a Nikon Coolpix 530 (1080/19:9, 1080/25p – 30 fps) was placed in a fixed position mounted on a tripod. In the second case, a DJI Mavik drone equipped with a full HD camera (1080/16:9; 1080/25p – 30 fps) was used. For each case, the position of the recording device was chosen according to the monitored area in order to contain the transect along which the benchmark ADCP profile was derived.

Marker panels, placed in clearly visible positions within the analysis areas, were used as Ground Control Points (GCPs) during orthoectification and stabilization phases. GCPs coordinates were acquired by a high-resolution differential GPS (Global Navigation Satellite System receiver device: Stonex S500).

2.3.2. Images processing

Considering the image spatial resolution and the maximum expected velocity for each case study, sub-pixel particle displacements could occur at the original acquisition frame-rate, negatively affecting the
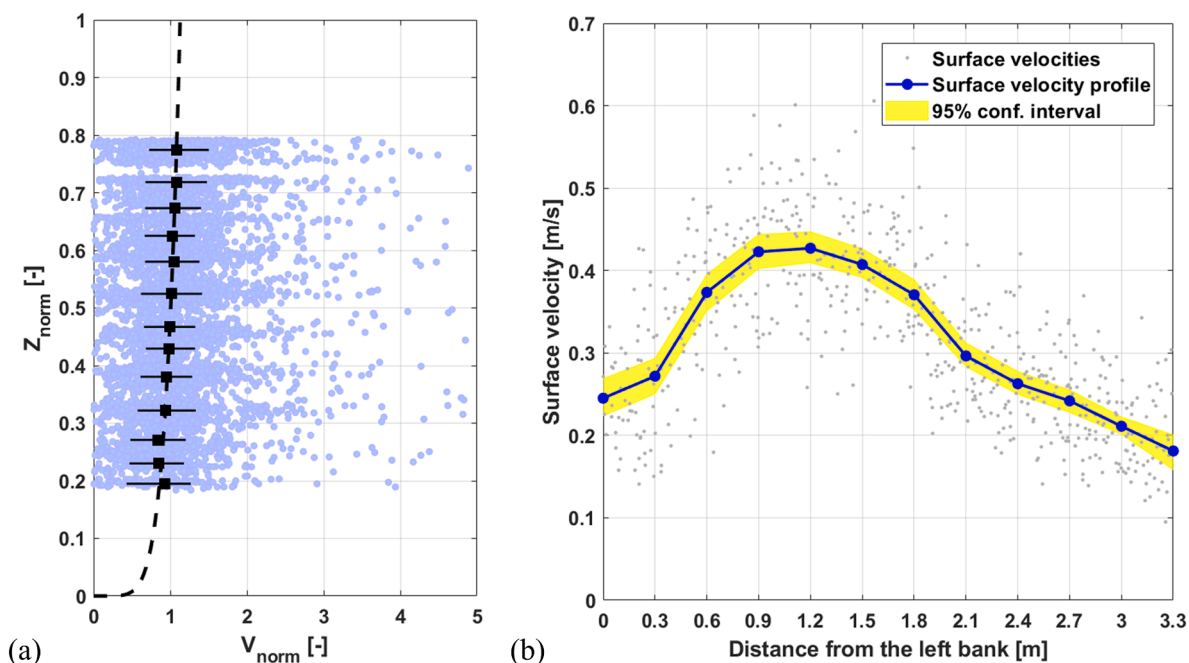
Fig. 2. PL-03. (a) Aggregated velocity data (blue points) collected at all the verticals of the retained transect-measurements, represented in a normalized graph. Median values at different depth intervals are reported by black square points, with indication of data dispersion for each interval through the visualization of the interquartile distance (horizontal solid black lines). Dashed black curve represents the normalized vertical velocity profile obtained by fitting a power law. (b) Surface velocity profile (blue line with circle markers) and 95% confidence interval (yellow bands) obtained from raw ADCP data. Grey points represent surface velocities obtained by power law interpolation at each vertical. (For interpretation of the references to color in this figure legend, the reader is referred to the web version of this article.)

detection procedure (Pumo et al., 2021). Frames extraction from the original acquired videos was thus performed reducing the processing frame-rate with respect to the acquisition frame-rate, i.e., from 30 to 15 fps.

The obtained frame sequences were then subjected to the pre-processing steps of stabilization and orthorectification. However, PIVlab is not equipped with stabilization and orthorectification algorithms, but it is featured with only a "Calibration" module through which the spatial and temporal resolution of the frames can be specified. For this reason, additional software were used to fulfil the pre-processing tasks. In particular, stabilization was applied using a highly performing module of the KLT-IV software (Perks, 2020), which uses the Good Features to Track algorithm (Shi and Tomasi, 1994) for the detection of the tracer movements, and the pyramidal Kanade Lucas Tomasi tracking scheme (Lucas and Kanade, 1981; Tomasi and Kanade, 1991), for the tracking process. In particular, considering a "dynamic" orientation of the camera used in the field campaigns, the "GCPs & Stabilization" option was chosen. In order to enhance the contrast between tracers and background, a greyscale transformation was finally applied by the stabilization algorithm (Tauro et al., 2017; Perks et al., 2020; Jolley et al., 2021), obtaining single-band images, with each pixel characterized by a Digital Number (DN) ranging from 0 (black) to 255 (white).

The last pre-processing step is the orthorectification of the stabilized and enhanced frames, used to correct perspective distortions and for images georeferencing. The "complete orthorectification" option was applied using a dedicated module of the FUDAA-LSPIV software (Le Coz et al., 2014).

When frames are acquired by drone (e.g., from a height around 20 m onwards), differences in the GCPs z-coordinate can be neglected assuming that GCPs lie onto the river surface plane (Jolley et al., 2021). If frames are recorded from a fixed location, the non-orthogonality of the camera lenses to the water surface introduces strong perspective distortions. Usually at least six not aligned GCPs are needed for frames heavily affected by perspective (Jodeau et al., 2008; Muste et al., 2008;

Detert, 2021), thus in all field case studies considered in this work, six GCPs were always ensured.

The processing phase was conducted through the freely available open-source PIVlab software (Thielicke and Stamhuis, 2014), developed in MATLAB environment. A Region of Interest (ROI) to which restrict the analyses was first identified, masking the portions of frames not occupied by liquid surface. The Fast-Fourier-Transform Cross-Correlation algorithm was selected for the statistical detection of the most probable frame-by-frame tracer displacement (frames processing style: 1–2, 2–3, 3–4, etc.). A total number of three passes were set, using linear interpolation option as window deformation interpolator. The size of the first Interrogation Area (IA_1) was selected equal to 32 px, following the guidelines from PIVlab developers (Thielicke and Stamhuis, 2014). The second and third passes width were calculated halving once and twice, respectively, the previous value (i.e., IA_2 16x16 px; IA_3 8x8 px).

Finally, a post-processing phase was applied using the Standard Deviation Test as vector validation algorithm. Denoting with $\overline{V}$ is the average velocity of the instantaneous surface velocity fields, and σ is the standard deviation, velocity vectors out of the range $\overline{V} \pm 2\sigma$ were rejected.

PIVlab uses a boundary value solver as interpolation algorithm, extrapolating missing data from the neighboring nodes through vertical, horizontal, and diagonal connections. As last post-processing step, the mean surface velocity field is obtained by temporally averaging node-by-node all the post-processed instantaneous velocity fields, also retrieving the surface velocity profile along the same transect considered for deriving the benchmark ADCP profile.

2.4. Automatic identification of the optimal processing sequence

The performances of LS-PIV based software programs are influenced by a wide range of factors. For instance, when tracer is manually introduced, operators have scarce control on the actual density and distribution of the tracer, which might become major sources of

uncertainty. Low tracer density and/or inhomogeneous spatial distribution of tracer particles could cause the occurrence of scarcely sampled portions of the investigated area, resulting in an incomplete and inaccurate representation of surface velocity fields. On the contrary, high tracer density could favor particles aggregation, disturbing cross-correlation algorithms. Density and distribution of the tracers can be, in turn, highly affected from several factors, such as the presence of wind, main currents and turbulence, and the disturbance effect of vegetation in the riverbed and banks.

Usually, seeding density and spatial distribution do not remain constant throughout the recording phase and some portions of video sequences might be not suitable for the subsequent LS-PIV phases. In such cases, it could be preferable to process only a limited portion of the acquired sequences, characterized by appropriate tracer properties. Pizarro et al. (2020b) introduced a metric, the SDI, able to characterize tracer density and its dispersion degree and whose formula was derived by considering numerical analyses on synthetic sequences generated under controlled tracer conditions. A features-detection algorithm (Dal Sasso et al., 2020) is used to compute SDI as a function of the frame-by-frame tracer density (expressed in particles-per-pixel, ppp) and the average spatial-clustering level, expressed as the average of ratios between the actual spatial-clustering level, i.e., ratio between variance and mean of the number of tracer particles, and an assumed reference distribution given by Poisson distribution, computed at different subareas of the ROI. The authors used the average SDI across several sub-sequences for the identification of the best (minimum SDI) and worst (maximum SDI) portion of a recorded video sequence.

The procedure proposed here is based on a metric analogous to the SDI, i.e., the global index GI, which is derived as a function of four indicators characterizing the spatial and temporal variability of tracer density and dispersion. The entire procedure is schematically described in Fig. 3. After a preliminary image sequence preparation, several sub-sequences are extracted from the original video through a moving window of varying duration. Tracer indicators are then computed, associated to each sub-sequence, and used to derive input variables for an Artificial Neural Network (ANN), which returns a numerical value of GI for each sub-sequence. Based on the obtained GI values, the procedure extracts the best sequence from the original video, corresponding to the sub-sequence with the minimum GI, also providing information about its initial frame position along the original video and its total number of frames.

2.4.1. Preliminary images sequence preparation and sub-sequences generation

The proposed methodology requires a further pre-processing step of graphic enhancement. A background removal (Elhabian et al., 2008) is then applied in order to maximize the contrast between tracer and background, favoring the characterization of the tracer density and distribution. With this purpose a video of the liquid surface, hereafter referred to as pre-seeding sequence, must be acquired immediately prior to the seeding process; the pre-seeding sequence duration is set equal to 10 s since it must be not too short to efficiently characterize the background, and not excessively long to minimize computational times and possible environmental (e.g., lighting) disturbance effects. The pre-seeding sequence must undergo the same pre-processing steps of the post-seeding video. An analysis on the pre-seeding frames is then performed, obtaining a reference background image by averaging DNs at each pixel of images over the entire pre-seeding sequence.

Once the reference background image is computed, the original post-seeding sequence is modified by subtracting, pixel-by-pixel, the associated DNs from the reference background image, and then applying a final stretching procedure through a binarization algorithm, with a binarization threshold ranging between 80 % and 90 % of 255 (8-bits) (Dal Sasso et al., 2021a). The obtained frame sequence contains Boolean images with tracer particles pixels assuming DNs equal to 1 (white) and background pixels with DNs equal to 0 (black).

The next step in the proposed procedure involves extracting a series of sub-sequences from the original video. Sub-sequences generation is performed using a moving window of given duration sliding along the binary sequence with a fixed time-lag. The procedure allows user to set multiple time-window durations and lags as parameters. The minimum duration should be chosen according to the expected tracer velocity,
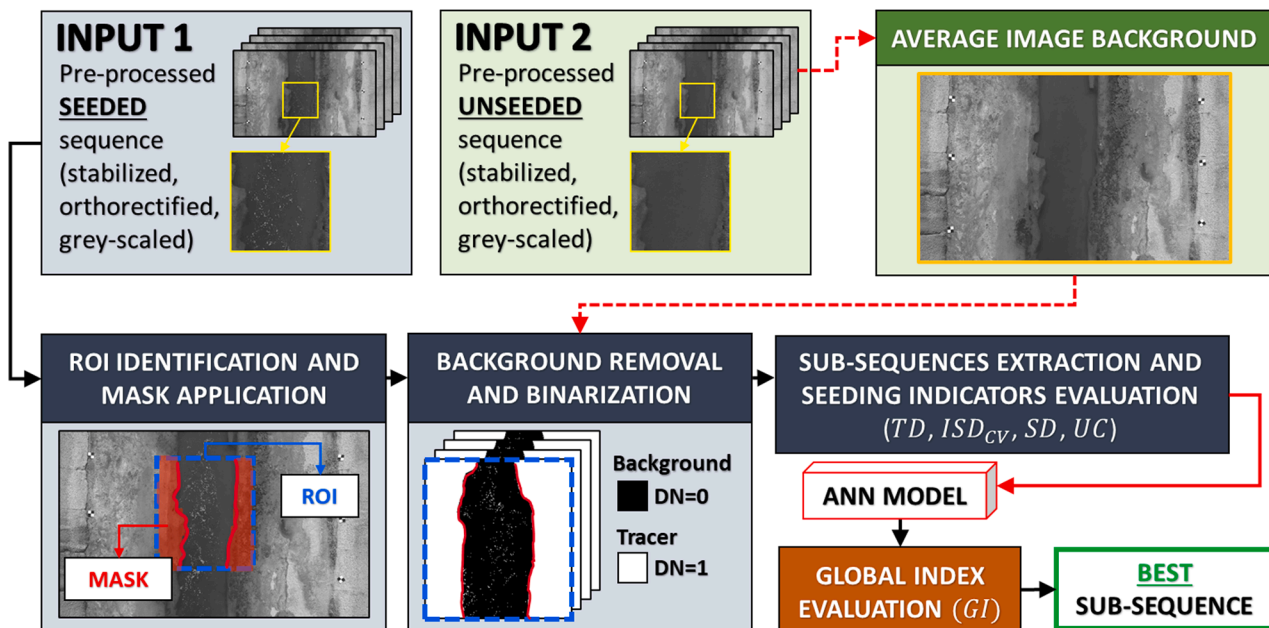

Fig. 3. Flowchart of the proposed procedure. Sequences recorded under pre- and post-seeding conditions, properly pre-processed, are used as input, with the latter used to derive an average background image. Considering a selected ROI, where a mask can be also applied to the useless portions of the frames, a combined enhancement-binarization procedure is applied to obtain Boolean images. Several sub-sequences are then extracted through a moving window of variable size, computing four indicators representative of the seeding conditions for each of them. These are used to force an ANN which provides the global index GI for each sub-sequence, useful to identify the best sub-sequence within the original available video, that is ultimately extracted for LS-PIV analysis.

while the maximum duration must not exceed the total length of the original video. Lag parameter might help to reduce computational times, avoiding redundancy due to excessively overlapping sub-sequences.

2.4.2. Characterization of each sub-sequence

An indicator representative of the tracer amount in the ROI of each frame, i.e., the Instantaneous Seeding Density (ISD$_i$), is defined, frame-by-frame, as the ratio between the total number of pixels within the ROI occupied by tracer, $n_{tr,i}$, and the total number of pixels of the ROI, $n_{ROI,i}$:

$$ISD_i = \frac{n_{tr,i}}{n_{ROI,i}} \tag{4}$$

with i referring to the generic i-th frame and ranging from 1 to the total number of frames in a recorded video, N_{fr}.

ISD_i is dimensionless and it increases with tracer density, ranging from 0 to 1. ISD_i is a proxy measure of the actual instantaneous seeding density in the ROI; nevertheless, incorrect interpretation of pixels (as tracer particle or background) can occur due to the approximate method adopted for binarization. This does not significantly influence the suitability of ISD_i for the purpose of the proposed procedure, which considers seeding density in relative terms to discriminate the various sub-sequences.

All the extracted sub-sequences are then characterized in terms of tracer properties through four, dimensionless indicators: (i) the Tracer Density index (*TD*), (ii) the coefficient of variation of ISD_i (ISD_{CV}), (iii) the Seeding Distribution index (*SD*), and (iv) the Undersampling Coverage index (*UC*). Such indicators are always greater than or equal to zero, with null values denoting optimal conditions.

The first two indicators are representative of the overall seeding density and its frame-by-frame variability across the analyzed sub-sequence, and they are derived from the frame-by-frame ISD_i. In particular, *TD* is obtained as:

$$TD = \left| ISD^* - ISD_{avg} \right| \tag{5}$$

where ISD_{avg} is the mean value of the ISD_i considering all the frames contained in each sub-sequence, while ISD^* represents an ideal reference value of tracer density. Dal Sasso et al. (2018) demonstrated via numerical experiments that for low tracer density, optical analyses performances increase with increasing tracer concentration, whereas no significant improvements can be noticed for density over to 0.01 ppp. It is worth noting that tracer concentrations significantly lower than 0.01 ppp are usually adopted in real field applications (Pearce et al., 2020; Dal Sasso et al., 2021b), whereas an excessive tracer density (e.g., more than 30 % of the surface area, according to Meselhe et al. (2004)) could lead to tracer aggregation, negatively affecting LS-PIV analyses. Here, a value of ISD^* equal to 0.2 was assumed, corresponding to the maximum value of ISD_i under conditions of no coalescence phenomena and particle size of the tracer uniform and equal to a pixel.

SD and *UC* are representative of the tracer spatial distribution over the ROI. More specifically, *SD* is derived adopting an Eulerian approach, first computing the relative frequency, f_P, of tracer occurrence in each pixel of the ROI over the entire sub-sequence, and then comparing it with the average value over all the pixels of the ROI, $\langle f_P \rangle$, representing, for given tracer density, the reference value of f_P under uniform spatial distribution of the tracer. In particular, *SD* is computed as a Root Mean Square Error (RMSE), where the residuals are defined by the differences between f_P and $\langle f_P \rangle$ at each pixel of the ROI:

$$SD = \sqrt{\frac{1}{n_{ROI}} \sum_{j=1}^{n_{ROI}} \left(f_{P,j} - \langle f_P \rangle \right)^2} \tag{6}$$

where j refers to the j-th pixel within the ROI.

UC is calculated as the fraction of pixels within the ROI classified as "under-sampled". The "under-sampled" condition in a specific pixel is established based on the relative frequency of tracer occurrence, f_P. In particular, a pixel is defined "under-sampled" when f_P is lower than a prefixed threshold value f_P^*, which was set equal to 0.01 as calibration parameter after performing a sensitivity analysis on a synthetic sequence, the same generated for the final test on the entire procedure that will be presented at Sect. 3.3 by exploring a range of f_P^* from 10^{-8} to 0.1; this implies, for instance, that for 60-second sub-sequences at 15 fps (i.e., 900 frames in total), a pixel is "under sampled" if it assumes DN equal to 1 for less than 9 frames.

2.4.3. Processing module for the identification of the best sub-sequence: Global index and ANN

Differently from the numerical approach used in Pizarro et al. (2020b), a data-driven empirical approach based on field data is used to derive the metric, i.e., the Global Index (GI), considered for the characterization of a sub-sequence in terms of seeding properties. In particular, GI is here obtained as a function of the four indicators described in the previous section, by mean of an ANN, opportunely designed, thus removing any a-priori assumption about the analytical form of the underlying relationships among the various seeding characteristics considered to characterize a sub-sequence.

All the sub-sequences with 30-, 60-, 90-, and 120-second durations (i. e., 450, 900, 1350, and 1800 frames at 15 fps, respectively) and lag of 2 s (corresponding to 45 frames at 15 fps), were extracted from the videos acquired at all the case studies, computing the four seeding indicators (*TD*, ISD_{CV}, *SD*, *UC*). The selected minimum duration considered for sub-sequences extraction ensures sufficient tracer dispersion within the ROIs for all the analyzed case studies, while the maximum duration was chosen equal to the shortest total duration of the acquired videos in all the case studies. Fig. 4 shows the obtained seeding indicators for all the 30-second and 120-second sub-sequences extracted for the case of PL-02, as demonstrative example. A portion of frame randomly extracted from both the best and the worst 30-second sub-sequences according to the TD indicator (i.e., minimum and maximum TD, respectively), is also visualized in the inset plots of Fig. 4, in order to highlight the existing differences in terms of seeding density.

Each extracted sub-sequence was analyzed applying the workflow described in Section 2.3.2, deriving the associated surface velocity profile along the transect where benchmark ADCP surface velocity profiles are available (see Section 2.2.2). ADCP surface velocity at the nodes of the PIVlab computational grid along the transect and corresponding PIVlab velocities were first retrieved, and the performance associated to each sub-sequence was measured comparing LS-PIV and ADCP velocity estimates through two different metrics: (i) the RMSE and (ii) the Willmott index, δ.

$$RMSE = \sqrt{\frac{1}{n_p} \sum_{k=1}^{n_p} \left(v_{PIVlab,k} - v_{ADCP,k} \right)^2} \tag{7}$$

$$\delta = 1 - \frac{\sum_{k=1}^{n_p} \left(v_{PIVlab,k} - v_{ADCP,k} \right)^2}{\sum_{k=1}^{n_p} \left(\left| v_{PIVlab,k} - \overline{v_{ADCP}} \right| + \left| v_{ADCP,k} - \overline{v_{ADCP}} \right| \right)^2} \tag{8}$$

where n_p refers to the total number of computational nodes along a transect, $v_{PIVlab,k}$ and $v_{ADCP,k}$ represent the surface velocity profile at the generic k-th computational node of the transect, and $\overline{v_{ADCP}}$ is the average velocity value of the benchmark profile. The dimensionless Willmott index (Willmott and Wicks, 1980; Willmott et al., 2012) allows for a direct comparison of results arising from different case studies; it can assume values ranging from zero (i.e., worst performances) to one (i.e., best performances).

The processing module of the proposed procedure is based on a Multi-Layer Perceptron Feedforward Artificial Neural Network (ANN), developed using the MATLAB ANN Toolbox. Two measurements, i.e.,
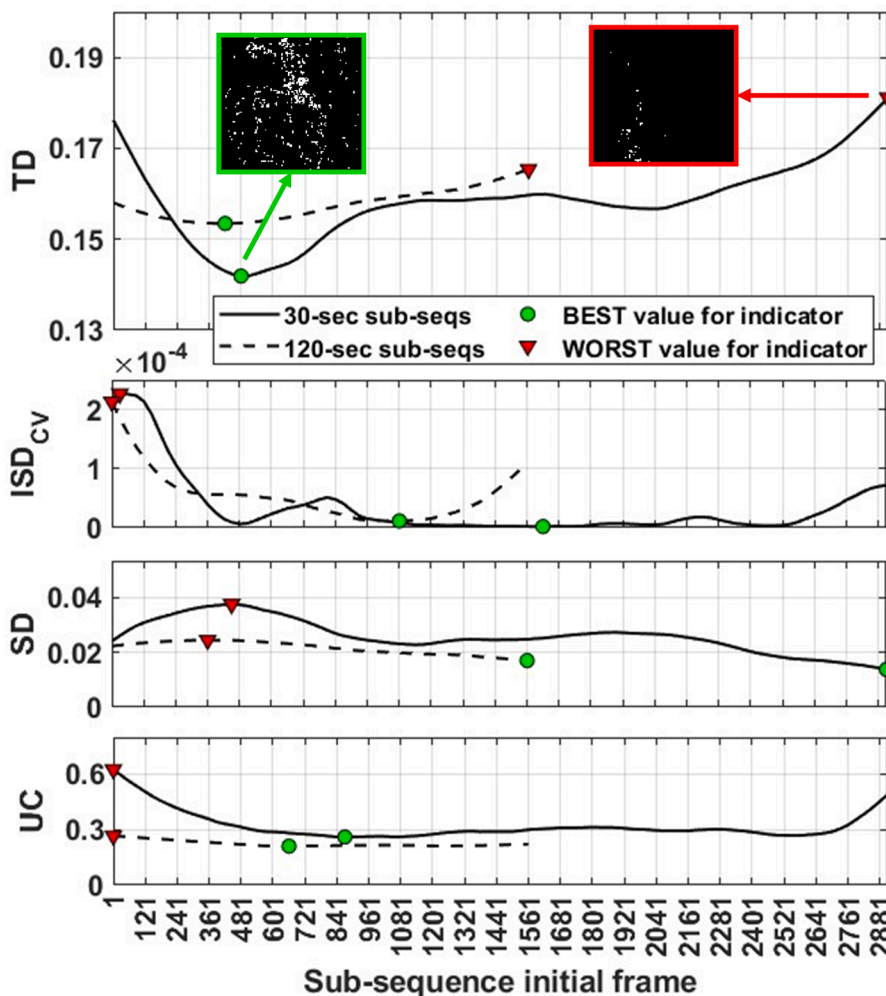
Fig. 4. Seeding indicators for the case PL-02. Indicators refer to sub-sequences extracted with a 30-second (solid lines) and 120-second (dashed lines) moving windows. X-axis refers to the initial frame of the sub-sequence with respect to the first acquired frame. Green circles and red triangles represent the sub-sequences characterized by the best (lowest) and worst (highest) value for each indicator, respectively. Equal sized portions of a frame randomly extracted from the 30-second sub-sequence with the lowest (green contour) and highest (red contour) TD are also reported in the inset plots. (For interpretation of the references to color in this figure legend, the reader is referred to the web version of this article.)

BEM-01 and PA-01, were excluded for the ANN training and will be used only for validation purposes. Data from the ten remaining measurements (i.e., calibration case studies) were considered to form a unique large database used to train the ANN. This last was obtained after aggregation of different "single-case" datasets derived from each calibration case study. Each sample of a "single-case" dataset refers to a specific sub-sequence and contains paired input–output variables; more specifically, as output "response" variable for the ANN it was considered the RMSE associated to the sub-sequence normalized by the mean RMSE of all the sub-sequences extracted for that case study, while five variables for each sub-sequence are used as paired input: the ISD_{avg} and the four seeding indicators (TD, ISD_{CV}, SD, UC) associated to the sub-sequence, these last after normalization with respect to the corresponding mean values over all the sub-sequences. From the analysis of the sub-sequences extracted at all the calibration case studies, a unique database containing 2780 samples was obtained after aggregation of all the "single-case" datasets.

An approach similar to that used in Pumo and Noto (2023) was adopted for the configuration and training of the ANN. A total of 395 different ANN topologies were explored, considering one or two Hidden Layers (HLs), and progressively varying the number of nodes in the first HL from 5 to 200 nodes and, in the case of two layers, fixing the number of nodes in the second HL equal to half of those in the first HL. The ANN

was trained using the "Levenberg-Marquardt" error backpropagation algorithm and considering the Mean Absolute Error (MAE) as loss function. The training adopted an early stopping criterion considering a random division of the dataset for training (70 % of data), validation (15 %) and testing (15 %) purposes. For each explored topology, a total of 100 training trials were performed, selecting for each structure that with the lowest MAE in validation. Once the "optimal" ANN topology was identified, as the one among all the tested configurations with the lowest MAE, a training refining was carried out performing further 1000 training trials under that configuration and selecting as final ANN the one with the lowest MAE in validation. The aforementioned procedure provided a final network with two HLs, having 135 nodes at the first HL and 67 at the second HL. Fig. 5 shows a schematic representation of the final ANN structure and the regression plot of the considered response variable, i.e., the normalized RMSE versus the simulated output variable, i.e., the GI, from which it is possible to notice a very high matching degree, with a coefficient of determination R^2 equal to 0.97.

No constraints were applied to the ANN output, so the GI can assume both positive and negative real values. When a sequence is passed to the automatic procedure and sub-sequences are extracted, the ANN evaluates all the GI associated to all the sub-sequences and selects the best sub-sequence as that corresponding to the lowest GI, which represents the most suitable for LS-PIV analyses. Given the considered response
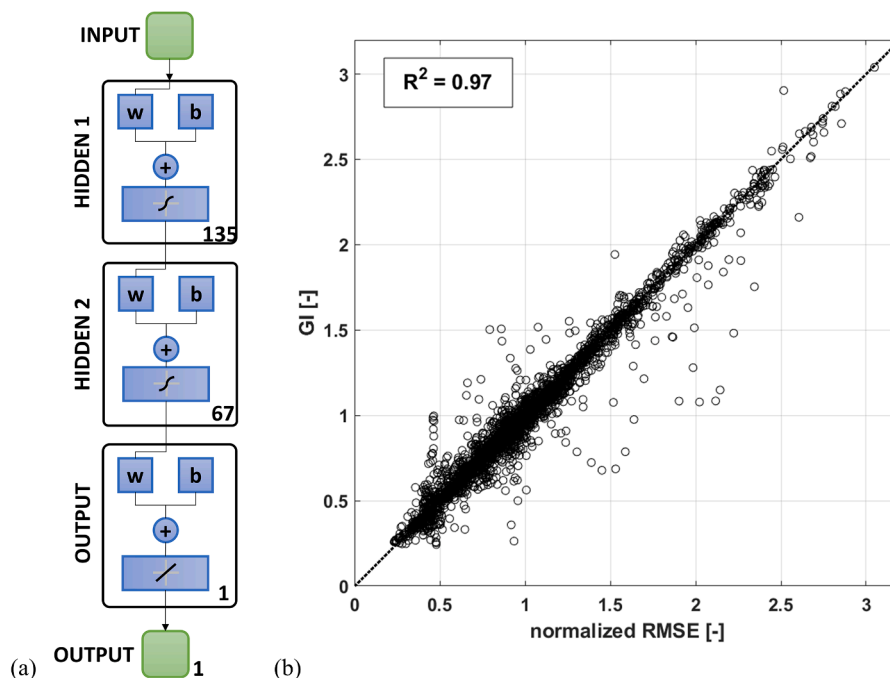
Fig. 5. (a) Schematic representation of the ANN model: Input Layer with 5 nodes (i.e., *TD*, *ISD_CV*, *SD*, *UC*, and *ISD_avg*), two HLs with 135 and 67 nodes at the first and second HL, respectively, and Output Layer with single node. The visualization of the ANN structure is derived from MATLAB. (b) Regression plot between normalized RMSE and GI over the entire dataset used for the ANN training. Dashed black line refers to the perfect matching.

variable, values of GI lower than unit denote performances better than the mean performances over all the sub-sequences.

3. Results

3.1. Application to the calibration case studies

The training dataset used to create the ANN was generated considering sub-sequences extracted from 10 out of 12 field case studies reported in Table 1 (see Sect. 2.4.3). The calibrated procedure is here applied to all the calibration case studies, and the results are summarized in Table 3. The RMSE values, evaluated by comparing LS-PIV and the corresponding ADCP surface velocity profiles, for the best sub-sequences according to the GI are significantly lower (on average −40 %) than those associated to the worst sub-sequences. The best case in terms of both RMSE and δ was OR-02, where the analysis of the optimal sub-sequence identified by the procedure led to RMSE equal to 0.026 m/s and δ equal to 0.92. For all the cases, the deviation of the RMSE associated with the best sub-sequence according to GI from the lowest achievable value (RMSE_min) is extremely low, i.e., on average

Table 3
Results at the calibration case studies (ID_m). The best and the worst performance indexes PI (PI_best and PI_worst, respectively) among all the sub-sequences of each case study, with indication of the minimum and maximum RMSE and δ. Characterization of the best and worst (in italic) sub-sequences identified according to GI, with indication of the associated GI, RMSE and δ, the sub-sequence duration (d_ss) and initial frame with respect to the first frame of the original video (fr_in).

ID_m	PI_best		PI_worst		GI	d_ss	fr_in	RMSE	δ
	RMSE_min	δ_max	RMSE_max	δ_min					
	[m/s]	[-]	[m/s]	[-]	[-]	[s]	[fr]	[-]	[m/s]	[-]
OR-01	0.052	0.72	0.095	0.39	0.76	30	450	1	0.061	0.65
					1.59	*30*	*450*	*2071*	*0.095*	*0.40*
OR-02	0.014	0.96	0.155	0.09	−1.08	30	450	1381	0.026	0.92
					2.44	*30*	*450*	*2671*	*0.153*	*0.12*
OR-03	0.048	0.85	0.130	0.45	0.58	90	1350	751	0.055	0.80
					1.72	*30*	*450*	*3451*	*0.130*	*0.45*
PL-01	0.060	0.59	0.114	0.34	0.26	30	450	781	0.068	0.51
					1.70	*30*	*450*	*2161*	*0.114*	*0.34*
PL-02	0.023	0.95	0.135	0.37	0.34	30	450	871	0.031	0.92
					2.90	*30*	*450*	*1*	*0.135*	*0.37*
PL-03	0.061	0.89	0.267	0.33	0.40	60	900	1	0.069	0.87
					2.13	*30*	*450*	*2701*	*0.262*	*0.35*
CA-01	0.068	0.73	0.132	0.37	0.81	120	1800	721	0.076	0.57
					1.60	*30*	*450*	*3061*	*0.131*	*0.51*
CA-02	0.053	0.65	0.156	0.20	0.59	30	450	511	0.058	0.65
					2.05	*30*	*450*	*1*	*0.155*	*0.39*
BEP-01	0.036	0.92	0.171	0.42	0.58	60	900	961	0.039	0.91
					2.05	*30*	*450*	*1*	*0.155*	*0.42*
IM-01	0.026	0.88	0.189	0.05	0.24	90	1350	241	0.031	0.81
					2.90	*30*	*450*	*2911*	*0.189*	*0.05*

equal to 0.007 m/s and never exceeding 0.012 m/s, demonstrating the suitability of the automatic procedure proposed in all the case studies. It can be also noticed that, as it was expected, the worst sub-sequences according to the GI are always associated to short sub-sequences (i.e., 30 s long, that is the lowest duration considered) extracted from the beginning or the ending part of the original video, when tracer is often not yet or no longer well dispersed over the entire area.

Fig. 6 shows for the same field case study used in Fig. 4 (i.e., PL-02), a comparison between tracer coverage maps relative to the best and the worst sub-sequences automatically identified by the procedure based on GI. The tracer coverage maps display the pixel-by-pixel values of the relative frequency of tracer occurrence over the entire ROI , f_P, which is a variable used for the computation of both SD and UC (Section 2.4.2). Tracer coverage maps provide clear insights on the density and the distribution of the tracer in space and time over the sub-sequence, with "under-sampled" pixels displayed in white, while pixel properly crossed by tracer displayed using a scale color bar. In the upper inset plots of Fig. 6, three frames extracted from the initial, middle, and final part of the sub-sequences are also visualized to further emphasize the differences between the best and the worst sub-sequences in terms of tracer density and spatial distribution. Moreover, the position of the reference transect, where performances indexes RMSE and δ are evaluated, is also reported within the tracer coverage maps by red lines.

The two sub-sequences identified at the selected PL-02 case by the procedure, are characterized by the same duration (i.e., 30 s, equal to 450 frames at 15 fps), GI equal to 0.34 for the best sub-sequence, and 2.90 for the worst one. The worst sub-sequence (Fig. 6b) was extracted from the beginning of the raw video, with initial frame of the sub-sequence corresponding to the first frame of the acquired video, while

the best sub-sequence was extracted starting from the 871st frame, i.e., from the central portion of the original video. From the tracer coverage map, it can be noticed how tracer for the worst sub-sequences remained mainly concentrated in the upstream portion of the ROI, with a density and spatial coverage increasing in time (see associated frames in the inset plots). The area along the transect was scarcely sampled causing weak performance indexes, since the tracer had not yet covered the entire frame. On the contrary, tracer for the best sub-sequence (Fig. 6a) was rather well distributed over the ROI, especially along the central area of the river, and not significant differences in terms of tracer density and spatial distribution can be noticed from the comparison among the frames reported in the inset plots, demonstrating that such conditions were stable over time along the sub-sequence; this indeed led to an adequate characterization of the surface velocity field by the LS-PIV approach and, consequentially, to much better values of the performance indexes compared to the worst sub-sequence, with RMSE passing from 0.135 m/s to 0.031 m/s and □ passing from 0.37 to 0.92. Comparison in Fig. 6 clearly shows the capability of the proposed procedure in identifying sub-sequences characterized by adequate and not adequate tracer density and spatial distribution based on the four indicators used to compute the GI, and, in fact, such indicators well describes the two sub-sequences shown in figure, with the best sub-sequences having more tracers ($TD = 0.154$ vs. 0.176), with density much less variable in time ($ISD_{CV} = 4.08E-5$ vs. 2E-4), and better distributed over the ROI ($SD = 0.036$ vs. 0.039, and $UC = 0.26$ vs. 0.63) compared to the worst sub-sequence (see also Fig. 4).

Fig. 7 shows, for the cases of OR-02 and BEP-01, a comparison among the ADCP benchmark profile (dashed blue lines) and all the PIVlab based surface velocity profiles (grey lines) derived from the processing of all
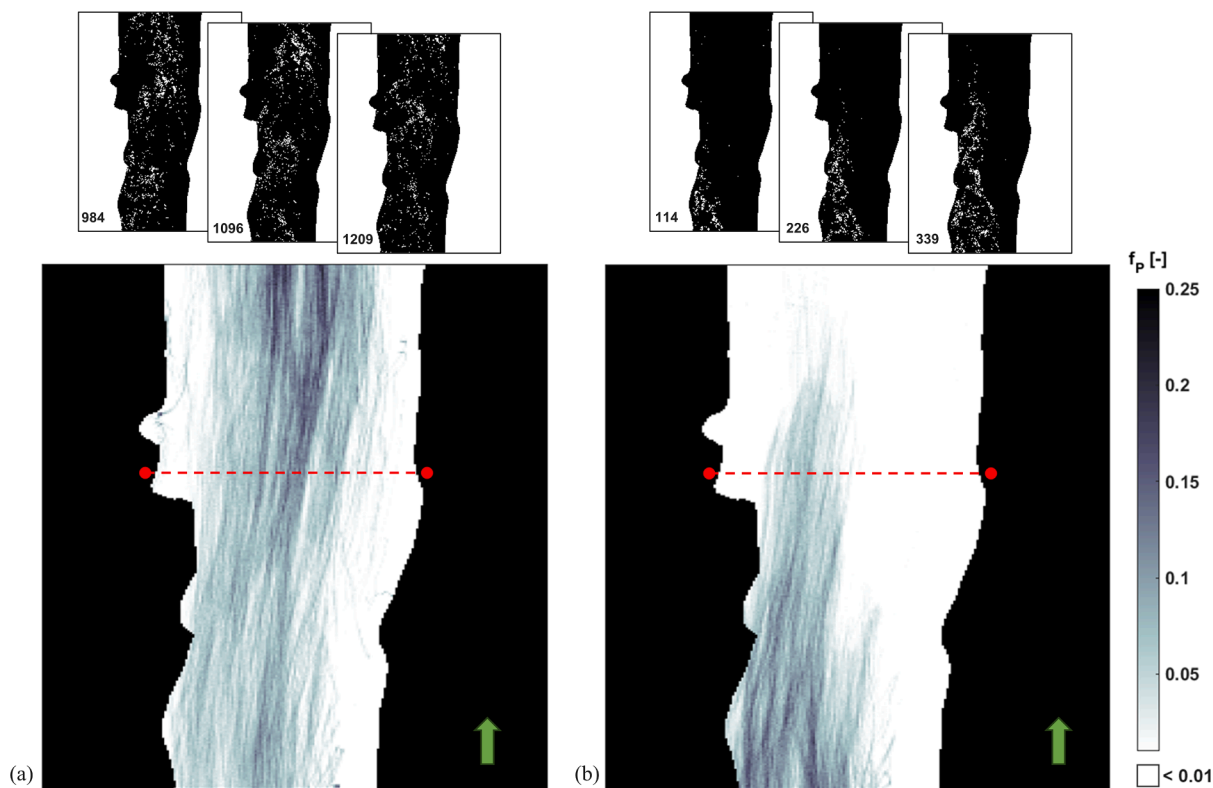

Fig. 6. Tracer coverage maps of (a) the best and (b) the worst sub-sequences identified by the automatic procedure at PL-02. White color denotes "under-sampled" pixels ($f_P < 0.01$). Tracer motion direction (green arrow) and the location of the reference transect (dashed red line) are also highlighted within the coverage maps. Three frames extracted at the 25 %, the 50 %, and the 75 % of the total duration of the two sequences are also reported in the inset plots (number in the corner refers to the progressive frame across the entire original video acquired at the case study). (For interpretation of the references to color in this figure legend, the reader is referred to the web version of this article.)
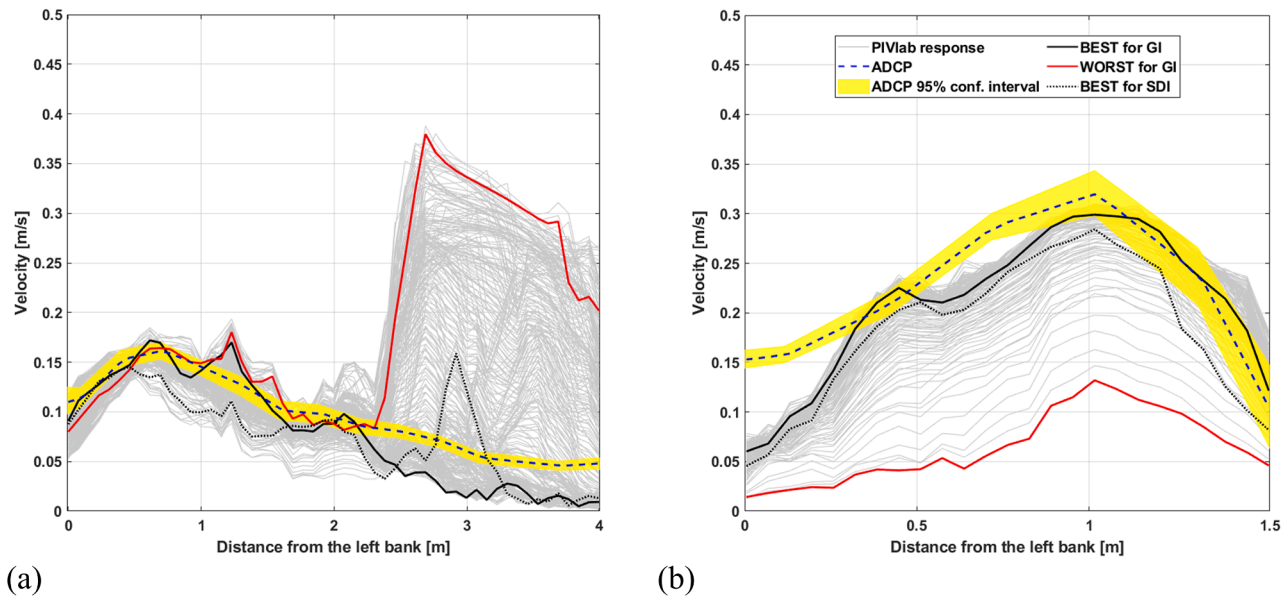
Fig. 7. Comparison between surface velocity profiles obtained by processing in PIVlab all the possible extracted sub-sequences from original videos (grey lines) and the ADCP benchmark profile (dashed blue lines) at the calibration case studies (a) OR-02 and (b) BEP-01. The 95% confidence intervals for ADCP benchmark profiles are also shown (yellow bands). Surface velocity profiles associated with the best and the worst sub-sequences according to the GI are underlined with the black and red solid lines, respectively, while dashed black lines refer to the best sub-sequence according to the SDI. In the x-axis the progressive distance from the left bank is shown, while the y-axis reports the surface velocity values in m/s. (For interpretation of the references to color in this figure legend, the reader is referred to the web version of this article.)

the sub-sequences extracted from original videos, with highlighted those corresponding to the best (black lines) and worst (red lines) sub-sequences according to the GI metric. The PIVlab based surface velocity profiles corresponding to the best sub-sequences according to the SDI metric by Pizarro et al. (2020b) (black dashed lines) are also highlighted in the same figure for comparison. The variability of the grey lines in Fig. 7 underlines the high sensitivity of the PIVlab response to the considered sub-sequence for each case study. Most of the LS-PIV based profiles for OR-02 (Fig. 7a) show large discrepancies with the benchmark velocity profiles close to the right riverbank, that could be due to two factors. The first reason is specific of the case under analysis, where differently from other cases, during the seeding activities, tracer was not uniformly distributed over the surface, leaving this region rather under-sampled compared to the central zone; the second reason could be addressed to the systematic underestimation of velocities operated by PIVlab software near the banks, known as border effects (Pumo et al., 2021). For both cases shown in Fig. 7, there is an underestimation of the velocities with respect to the benchmark velocity profile, with the largest errors localized near the riverbanks. It is worth noting how for both cases, the best sub-sequences according to SDI are characterized by an error higher than those relative to the best sub-sequences identified

by the proposed procedure based on GI.

3.2. Validation of the procedure

In order to test the generalizing ability of the ANN and the transferability of the proposed methodology, the procedure was applied on two independent validation cases, totally neglected for the procedure setup, which are the BEM-01 and PA-01 case studies, also described in Table 1. Performance resulting from the PIVlab processing of the best and worst sub-sequences according to the GI and the SDI are compared in Table 4 and Fig. 8.

All the extracted (best and worst) sub-sequences have a total length of 30 s, except for the best sub-sequence according to the GI at the PA-01, which has a length of 120 s sub-sequence. It is worth noting that, for both cases, the best and the worst sub-sequences identified based on GI are not corresponding to those identified based on SDI. The advantages of considering the GI rather than the SDI as metric to select the best sub-sequences are evident for the case BEM-01, where similar performance indexes were found for the best and the worst sub-sequences identified via SDI, which are slightly higher than those associated to the worst sub-sequences according to GI, whereas much better performance indexes

Table 4
Total duration d_{ss} (expressed both in seconds and total number of frames), initial frame (fr_{in}), RMSE and δ for the best and worst sub-sequences according to the GI (proposed procedure) and the SDI (Pizarro et al., 2020b) at the two validation cases (i.e., BEM-01 and PA-01). Associated GI and SDI are also reported, with the lowest and highest values highlighted in bold and italic, respectively. The lowest and highest values of the performance indexes (i.e., RMSE and δ) among all the sub-sequences extracted for each case are also displayed below the ID_m.

| ID_m		GI	SDI	d_{ss}		fr_{in}	RMSE	δ
		[-]	[-]	[s]	[fr]	[-]	[m/s]	[-]
BEM-01	best for GI	**0.58**	6.08	30	450	1441	0.057	0.50
$RMSE_{min} = 0.050\ m/s,\ \delta_{max}=0.53$	best for SDI	1.20	**4.61**	30	450	901	0.111	0.23
$RMSE_{max} = 0.185\ m/s,\ \delta_{min}=0.14$	worst for GI	*2.29*	9.70	30	450	1	0.185	0.15
	worst for SDI	1.33	*61.07*	30	450	2731	0.112	0.26
PA-01	best for GI	**0.41**	0.57	120	1800	361	0.005	0.99
$RMSE_{min} = 0.005\ m/s,\ \delta_{max}=0.99$	best for SDI	2.65	**0.45**	30	450	1	0.027	0.80
$RMSE_{max} = 0.029\ m/s,\ \delta_{min}=0.79$	worst for GI	*2.74*	0.46	30	450	121	0.029	0.79
	worst for SDI	1.35	*0.89*	30	450	2101	0.014	0.93
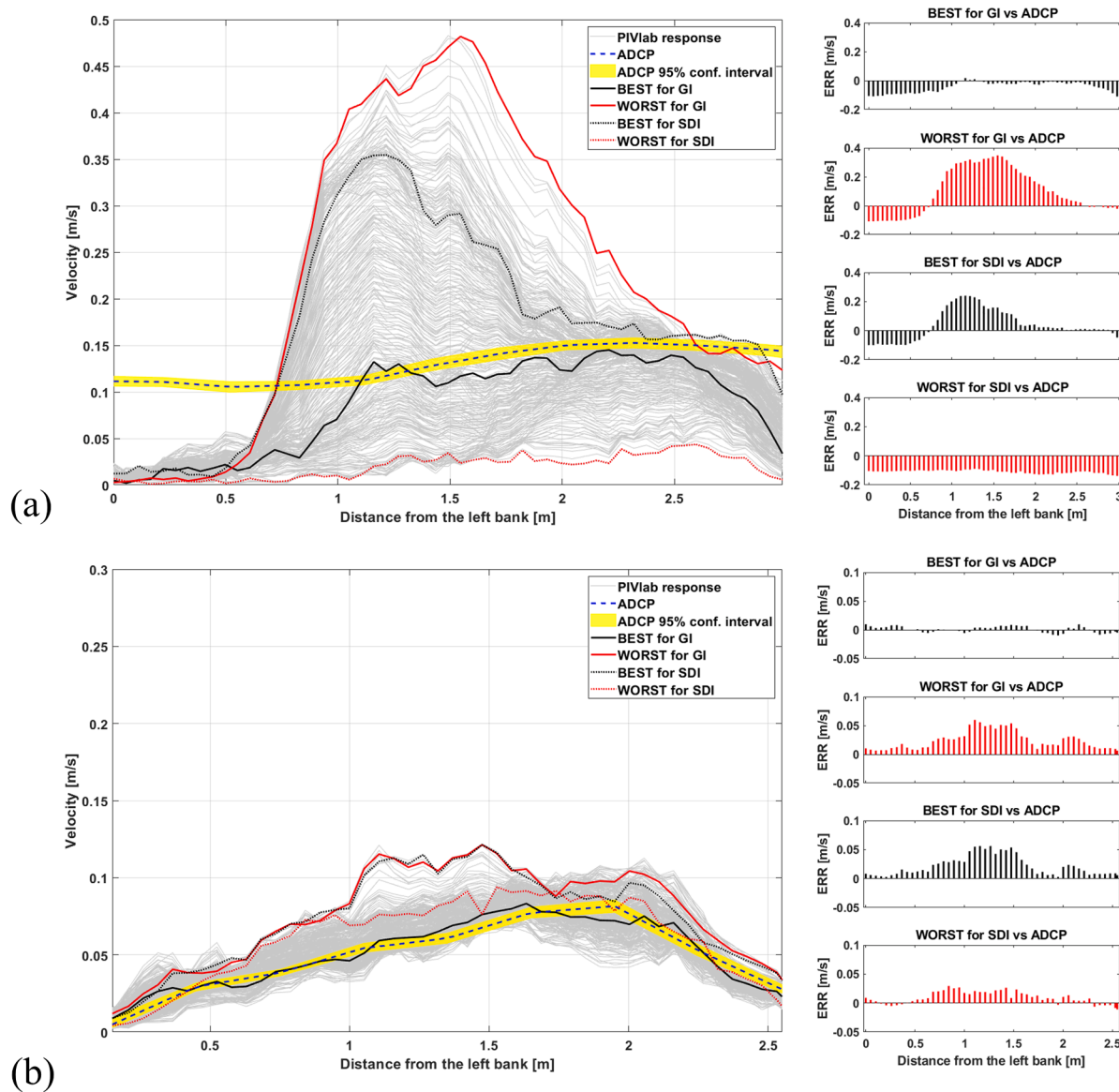
Fig. 8. Surface velocity profiles comparison (left plots) at the (a) BEM-01 and (b) PA-01 validation case studies: blue dashed lines refer to ADCP benchmark profiles; grey solid lines refer to LS-PIV profiles; profiles for the best (black lines) and the worst (red lines) sub-sequences identified based on GI (solid lines) and SDI (dashed lines) are highlighted; 95% confidence intervals of the ADCP profiles are also reported. Right plots display error bars derived for the best and worst sub-sequences based on GI and SDI. (For interpretation of the references to color in this figure legend, the reader is referred to the web version of this article.)

were found for the best sequence identified using GI (Table 4). This demonstrates the higher efficiency of the GI in identifying both the best and the worst sub-sequences compared to the SDI metric. Similar considerations can be made for PA-01, where PIVlab processing of all the extracted sub-sequences provided always surface velocity profiles rather close to the benchmark ADCP profiles; in this case, the best and the worst sub-sequences selected by the proposed procedure are corresponding to the sub-sequences with the best (lowest RMSE and highest δ) and the worst (highest RMSE and lowest δ) performances, respectively, among all the sub-sequences analyzed, while the sub-sequences selected based on SDI showed a counter intuitive behavior, with the worst sub-sequence (minimum SDI) having performances better than the best sub-sequence (maximum SDI).

Fig. 8, analogously to Fig. 7, shows the comparison between the surface velocity profiles for the two validation cases; bars error plots displayed on the right refer to the comparison between the ADCP benchmark profile and the PIVlab profiles associated to the best and the worst sub-sequence according to both GI and SDI.

For BEM-01 (Fig. 8a), the LS-PIV surface profile of the best GI sub-sequence follows the ADCP benchmark profile in the middle part, showing high percent errors with respect to benchmark values mainly along the banks (−98 % and −77 % for the left and right banks, respectively) and an overall slight underestimation of the mean surface velocity. On the contrary, the procedure based on SDI fails in detecting the optimal sub-sequence, with the profile associated to the best sub-sequence according to SDI characterized by an overestimation of the surface velocities along most of the transect and maximum percent error around 200 % in central nodes. Performances associated to the best and worst sub-sequence based on SDI for BEM-01 are rather similar with each other, with RMSE and δ almost two times those corresponding to the best GI sub-sequence (Table 4).

For PA-01 (Fig. 8b), the LS-PIV surface profile of the best GI sub-sequence shows an almost perfect matching with the corresponding benchmark ADCP profile (RMSE equal to 0.005 m/s and δ equal to 0.99), closely following the entire profile, with alternating under- and over-estimations of the velocity throughout the transect never exceeding

0.009 m/s. Greater errors are obtained considering the surface velocity profile of the best sub-sequence for SDI, where a maximum over-estimation of 0.056 m/s was reached.

The application of the proposed method to both the validation cases confirmed performances similar to those obtained through the applications to the calibration case studies, also highlighting how the procedure based on the GI metric outperforms that based on SDI, since it is more efficient in identifying the most and the least suitable sub-sequences for LS-PIV analysis within the original sequence.

3.3. Test under controlled conditions

A numerical experiment has been carried out with the aim to test the proposed methodology under flow velocity and tracer density conditions significantly different from those characterizing the field measurements used to build the ANN-based processing module. Using the Image Sequence Generator (ISG) described in Pumo et al. (2021), two 15-min synthetic image sequences with temporal resolution of 15 fps and spatial resolution of 0.003 m/px were generated, setting circular tracer particles with constant diameter of 10 px randomly dispersed over a ROI of 600 × 600 px. The first half of each sequence is characterized by a tracer uniformly distributed over the ROI and density linearly increasing from 0.013 ppp to 0.104 ppp, corresponding to half and four times, respectively, the average density derived from the real field case studies (0.026 ppp). The second half of the sequences considers the same tracer density variations, but its spatial distribution is disturbed deliberately leaving from 1/6 to 1/3 of the ROI uncovered by tracer. The unseeded areas position varies along the sequence in a loop modality, including: i) the area close to both the banks first; ii) then the area close to only a bank at a time (left first and then right); and iii) finally the central area of the ROI. Tracer particles 1-D motion is simulated applying a uniformly velocity profile along the direction of water current. More specifically, tracer velocity was set constant over the entire sequences, imposing a realistic logarithmic velocity profile along the cross section, with peak velocity in the middle section and lower velocities close to the banks. For the first sequence an average velocity of 0.5 m/s was set, while the second considers an average velocity of 2 m/s, so that both values are consistently higher than the mean velocities observed during the field surveys (Table 2).

Synthetic sequences do not consider disturbances phenomena to which real sequences are naturally subject (e.g., changes in lights, wind, rain, glares, turbulent eddies, tracer coalescence phenomena, vegetation, etc.). Tracer particles generated by ISG are regular in shape and constant in size, and their movement is not disturbed by turbulent eddies and has no transverse components. It is worth noting that even using the most complex image sequences generators, it is not possible to faithfully reproduce the high variability of the real cases characteristics considering the high influence of disturbing factors. More details about the ISG can be found in the original paper (Pumo et al., 2021).

The automatic procedure was applied to the two synthetic image sequences, extracting and processing all the possible sub-sequences with duration of 30, 60, 90, and 120 s, and time-lag equal to 2 s. For each sub-sequence, the procedure evaluated the seeding indicators described in Sect. 2.4.2, deriving the associated GI through the ANN and retrieving the sub-sequence with the lowest GI as the most suitable sub-sequence for LS-PIV analysis.

Fig. 9 show the full range of PIVlab surface velocity profiles (grey lines) obtained after processing all the extracted sub-sequences for each synthetic case. The profiles associated to the best and the worst sub-sequences in terms of GI are highlighted in black and in red, respectively, while imposed velocity by the ISG is also reported for comparison by blue markers.

The variability of the PIVlab response over the various sub-sequences is much less evident than for the real cases, since, for synthetic cases, it depends exclusively on the different tracer density and distribution, while in real cases it is also affected by other disturbance effects, inev-
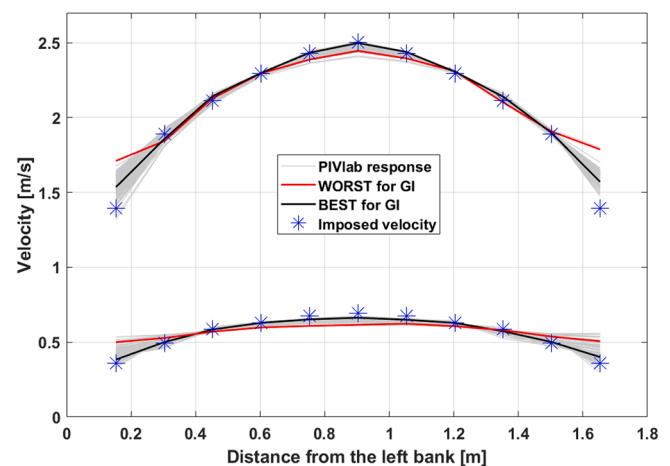

Fig. 9. Comparison between the velocity imposed in the ISG (blue star markers) for the generation of two synthetic image sequences, and the PIVlab surface velocity profiles obtained by processing all the sub-sequences extracted for each synthetic sequence (grey lines). The best (lowest GI, black lines) and the worst (highest GI, red lines) surface velocity profiles identified by the automatic procedure are also reported. Upper graph refers to the synthetic image sequence with average surface velocity of 2 m/s, while bottom graph refers to the synthetic sequence with average velocity of 0.5 m/s. (For interpretation of the references to color in this figure legend, the reader is referred to the web version of this article.)

itably present despite the application of graphical enhancement pre-processing procedures. Results shown in Fig. 9 confirm the reliability of the proposed procedure also under conditions rather far from those considered to train the ANN core module and experienced during the real field measurements campaign. For both the synthetic sequences tested, the best sub-sequences detected by the proposed procedure are characterized by surface velocity profiles in satisfying agreement with the ISG imposed surface velocity profiles, with an error evaluated in terms of RMSE near to the lowest RMSE over all the sub-sequences (0.020 m/s vs 0.014 m/s for faster case, and 0.072 m/s vs 0.035 m/s for slower case). At the same time, the worst sub-sequences show RMSE values close to the highest RMSE over all the sub-sequences (0.072 m/s vs 0.084 m/s for the faster case, and 0.153 m/s vs 0.154 m/s for the slower case), providing the highest error along the riverbanks. In terms of δ, the best sub-sequences detected for both the synthetic cases also show an almost perfect agreement with ISG imposed profiles, with values equal to 0.99.

4. Discussion

The proposed work is aimed to the development of operative procedures for field applications of optical techniques. Considering the critical influence that seeding density (Liu et al., 2021; Pumo et al., 2021; Bandini et al., 2022) and distribution (Dal Sasso et al., 2020, 2021a) may have in the optical software response, the proposed procedure represents an useful and practical instrument with the potentiality of automatically detecting an optimal portion of a recorded video sequence in terms of tracer characteristics for LS-PIV analyses. This tool can be considered as a fundamental component of the pre-processing phase in the workflow of image-based analyses. From the application of the proposed procedure to the 12 field measurements considered in this study, in fact, it is possible to notice that processing the best sub-sequence automatically extracted at each case rather than processing the entire available sequence leads to a percent reduction of the RMSE, on average, equal to 65 %. The main practical implication is that the best sub-sequences identified by the proposed procedure may have an information content higher than the entire sequences from which they are extracted. The identification of a smaller sequence, characterized by the

best compromise in terms of seeding density and distribution conditions, both in space and time, potentially allows for removing from the analyses scarcely sampled frames that may disturb the overall surface velocity field reconstruction, for example discarding the initial and final portions of the sequence, which are usually affected by a reduced presence of tracer with not well distributed patterns. This could allow for a significant improvement in the ability of LS-PIV software to reproduce velocity profiles, especially when tracer is artificially and manually introduced and there is scarce control on the seeding procedure.

The procedure basically extends an existing approach by Pizarro et al. (2020b), using a different and more complete metric for the seeding characterization and the consequent best sub-sequence identification and integrating the entire modeling chain in a unique algorithm coded in MATLAB environment. In particular, the SDI index used in Pizarro et al. (2020b), is obtained by an a-priori imposed functional exponential relationship between two seeding indicators of tracer density and distribution, calibrated numerically exclusively using synthetic sequences generated under controlled conditions.

The characterization of the seeding conditions of an images sequence is evaluated in the present work in a more comprehensive manner; the metric here adopted, the GI, is in fact based on four seeding characteristics, with two (i.e., *TD* and *SD*) rather similar to those used to compute the SDI and describing the spatial variability of seeding characteristics, and two further indicators that allow for taking into account also the temporal variability of tracer density (ISD_{CV}) and its spatial distribution (UC) along the processed image sequence. Differently from the SDI, the GI does not describe the mean density and distribution of tracer in a sequence, but rather it is a "state variable" that must be evaluated only in relative terms, comparing the different values associated to all the sub-sequences that can be extracted from the original video. Thus, the GI essentially measures, in relative terms, the suitability for LS-PIV analysis of a sub-sequence as a function of its seeding conditions. The relationship between LS-PIV performances and the seeding characteristics is here derived empirically, using a data-driven soft computing-based approach and exploiting a variety of field case studies, characterized by different conditions in terms of shape of cross-section, roughness of the channel bed and banks, vegetation, flow regime, and other environmental and hydraulic features.

The direct comparison between approaches using as discriminator metric for the seeding status, the SDI and the GI, has demonstrated the superiority of the empirically based method proposed. In many cases, the sub-sequence with the lowest SDI was not the actual best sub-sequence, corresponding to the sub-sequence allowing for the most accurate surface velocity field reconstruction after LS-PIV processing. Moreover, in some cases, the sub-sequences with the lowest and highest SDI provided similar accuracy or even counterintuitive results. On the contrary, the surface velocity profiles associated to the optimal sub-sequence based on GI have always shown a high matching degree with the reference ADCP profile, with performances very close or coincident with best achievable at each case, and always better than that corresponding to sub-sequence with the highest GI.

The core module of the procedure is an ANN that was trained with a rather wide number of field measurements. Nevertheless, the velocity characterizing the considered case studies were all representative of low flow conditions, with rather low average values, and this is probably the strongest limitation of the proposed approach. Despite the suitability of the procedure for higher velocity conditions was here successfully tested numerically, using properly generated synthetic sequences, the proposed approach could benefit from a future recalibration once other field measurements under high velocity conditions will be available.

5. Conclusions

Optical techniques are promising methods that allow for integrating or replacing traditional approaches to the river monitoring, offering a series of relevant advantages; they are low-cost, non-intrusive measurement techniques, permitting to acquire measures also when traditional methods cannot be applied, such as during floods.

In this paper we focused on the LS-PIV technique, which is one of the most used optical techniques for river monitoring in field applications. Many pre-processing operations can significantly improve the accuracy of cross-correlation algorithms, which represent the core modules of the most common LS-PIV based software. The performances of such programs are strictly dependent on the tracer conditions of the analyzed images sequence in terms of density and distribution in space and time. Ensuring proper seeding conditions in field measurements is often a hard challenge, due to the scarce control in the seeding process, especially when tracer is manually introduced. Many studies, including the present one, have demonstrated how processing only a limited and better seeded portion of the entire video recorded rather than the entire available sequence may considerably improve LS-PIV software performances.

This study has proposed a new procedure, accounting for the characteristics and time–space variability of the tracer along the entire acquired video, which allows for identifying and extracting automatically the most suitable sub-sequence for LS-PIV applications. The methodology was developed empirically, using data acquired from several field measurements for which benchmark ADCP surface velocity profiles were also available for specific transects. The procedure is based on a Global Index, GI, derived through an artificial neural network (ANN) as a function of different indicators characterizing the seeding conditions over the full examined sub-sequence, and it is aimed to identify among all the sub-sequences extractable from a case study that most suitable for LS-PIV analysis.

The application of the procedure to ten different calibration case studies has demonstrated the high reliability of the method and its potentialities in improving LS-PIV based reconstruction of the surface velocity profiles. The suitability of the procedure under conditions different from those experienced in the cases considered for the generation of the procedure was also successfully tested on two independent real case studies and using synthetically generated image sequences, with performance in validation similar to those achieved in calibration. The procedure developed is very simple and quick, and it could be particularly useful for all the cases where environmental and hydraulic conditions could negatively influence seeding motion, resulting in not constant and well-distributed particle patterns. The ability of the procedure in isolating the best portion of raw videos recorded during field measurement campaigns, in terms of seeding density and its distribution, has also a beneficial effect on the estimation of the discharge in a specific section of the river, reducing the overall uncertainty related to the estimation of surface velocities. Although the proposed procedure was implemented using LS-PIV technique, it could potentially support also other optical methods; for example, future research could be aimed at quantifying the benefits obtainable in Large-Scale Particle Tracking Velocimetry applications.

CRediT authorship contribution statement

Francesco Alongi: Conceptualization, Methodology, Validation, Writing – review & editing, Visualization, Writing – original draft, Investigation, Resources, Data curation, Software, Formal analysis, Writing – original draft. **Dario Pumo:** Supervision, Project administration, Funding acquisition, Conceptualization, Methodology, Validation, Writing – review & editing, Visualization, Writing – original draft, Investigation, Resources, Data curation, Software, Formal analysis, Writing – original draft. **Carmelo Nasello:** Investigation, Resources, Data curation. **Salvatore Nizza:** Investigation, Resources, Data curation. **Giuseppe Ciraolo:** Supervision, Project administration, Funding acquisition, Conceptualization, Methodology, Validation, Writing – review & editing, Visualization. **Leonardo V. Noto:** Supervision, Project administration, Funding acquisition, Conceptualization, Methodology, Validation, Writing – review & editing, Visualization.

Declaration of Competing Interest

Data availability

Data will be made available on request.

Acknowledgments

References

Acharya, A.S., Lowe, K.T., Ng, W.F., 2021. Fluorescent PIV using Atomized Liquid Particles. ISPIV21 1. doi: 10.18409/ispiv.v1i1.61.

Bandini, F., Lüthi, B., Peña-Haro, S., Borst, C., Liu, J., Karagkiolidou, S., Hu, X., Lemaire, G.G., Bjerg, P.L., Bauer-Gottwein, P., 2021. A drone-borne method to jointly estimate discharge and manning's roughness of natural streams. Water Res. 57 https://doi.org/10.1029/2020WR028266.

Bandini, F., Frías, M.C., Liu, J., Simkus, K., Karagkiolidou, S., Bauer-Gottwein, P., 2022. Challenges with regard to unmanned aerial systems (UASs) measurement of river surface velocity using doppler radar. Remote Sens. (Basel) 14, 1277. https://doi.org/10.3390/rs14051277.

Bodart, G., Le Coz, J., Jodeau, M., Hauet, A., 2022. Synthetic river flow videos for evaluating image-based velocimetry methods. Water Resour. Res. 58 https://doi.org/10.1029/2022WR032251.

Costa, J.E., Cheng, R.T., Haeni, F.P., Melcher, N., Spicer, K.R., Hayes, E., Plant, W., Hayes, K., Teague, C., Barrick, D., 2006. Use of radars to monitor stream discharge by noncontact methods: NONCONTACT STREAMFLOW. Water Resour. Res. 42 https://doi.org/10.1029/2005WR004430.

Creutin, J.D., Muste, M., Bradley, A.A., Kim, S.C., Kruger, A., 2003. River gauging using PIV techniques: a proof of concept experiment on the Iowa River. J. Hydrol. 277, 182–194. https://doi.org/10.1016/S0022-1694(03)00081-7.

Dal Sasso, S.F., Pizarro, A., Samela, C., Mita, L., Manfreda, S., 2018. Exploring the optimal experimental setup for surface flow velocity measurements using PTV. Environ. Monit. Assess. 190, 460. https://doi.org/10.1007/s10661-018-6848-3.

Dal Sasso, S.F., Pizarro, A., Manfreda, S., 2020. Metrics for the quantification of seeding characteristics to enhance image velocimetry performance in rivers. Remote Sens. (Basel) 12, 1789. https://doi.org/10.3390/rs12111789.

Dal Sasso, S.F., Pizarro, A., Manfreda, S., 2021a. Recent advancements and perspectives in UAS-based image velocimetry. Drones 5, 81. https://doi.org/10.3390/drones5030081.

Dal Sasso, S.F., Pizarro, A., Pearce, S., Maddock, I., Manfreda, S., 2021b. Increasing LSPIV performances by exploiting the seeding distribution index at different spatial scales. J. Hydrol. 598, 126438 https://doi.org/10.1016/j.jhydrol.2021.126438.

Detert, M., 2021. How to avoid and correct biased riverine surface image velocimetry. Water Res. 57 https://doi.org/10.1029/2020WR027833.

Detert, M., Weitbrecht, V., 2015. A low-cost airborne velocimetry system: proof of concept. J. Hydraul. Res. 53, 532–539. https://doi.org/10.1080/00221686.2015.1054322.

Elhabian, S.Y., El-Sayed, K.M., Ahmed, S.H., 2008. Moving object detection in spatial domain using background removal techniques-state-of-art. Recent Pat. Comput. Sci. 1, 32–54.

Fujita, I., Muste, M., Kruger, A., 1998. Large-scale particle image velocimetry for flow analysis in hydraulic engineering applications. J. Hydraul. Res. 36 (3), 397–414.

Hauet, A., Creutin, J.-D., Belleudy, P., 2008. Sensitivity study of large-scale particle image velocimetry measurement of river discharge using numerical simulation. J. Hydrol. 349, 178–190. https://doi.org/10.1016/j.jhydrol.2007.10.062.

Hauet, A., Morlot, T., Daubagnan, L., Paquier, A., Rivière, N., 2018. Velocity profile and depth-averaged to surface velocity in natural streams: a review over a large sample of rivers. E3S Web Conf. 40, 06015.

Herschy, R., 1995. General purpose flow measurement equations for flumes and thin plate weirs. Flow Meas. Instrum. 6 (4), 283–293.

Ioli, F., Pinto, L., Passoni, D., Nova, V., Detert, M., 2020. EVALUATION OF AIRBORNE IMAGE VELOCIMETRY APPROACHES USING LOW-COST UAVS IN RIVERINE

ENVIRONMENTS. Int. Arch. Photogramm. Remote Sens. Spatial Inf. Sci. XLIII-B2-2020, 597–604. doi: 10.5194/isprs-archives-XLIII-B2-2020-597-2020.

Jodeau, M., Hauet, A., Paquier, A., Le Coz, J., Dramais, G., 2008. Application and evaluation of LS-PIV technique for the monitoring of river surface velocities in high flow conditions. Flow Meas. Instrum. 19, 117–127. https://doi.org/10.1016/j.flowmeasinst.2007.11.004.

Jolley, M.J., Russell, A.J., Quinn, P.F., Perks, M.T., 2021. Considerations when applying large-scale PIV and PTV for determining river flow velocity. Front. Water 3, 709269. https://doi.org/10.3389/frwa.2021.709269.

Junqueira, A.M., Mao, F., Mendes, T.S.G., Simões, S.J.C., Balestieri, J.A.P., Hannah, D. M., 2021. Estimation of river flow using CubeSats remote sensing. Sci. Total Environ. 788, 147762 https://doi.org/10.1016/j.scitotenv.2021.147762.

Koutalakis, P., Zaimes, G.N., 2022. River flow measurements utilizing UAV-based surface velocimetry and bathymetry coupled with sonar. Hydrology 9, 148. https://doi.org/10.3390/hydrology9080148.

Lagogiannis, S., Dimitriou, E., 2021. Discharge Estimation with the Use of Unmanned Aerial Vehicles (UAVs) and Hydraulic Methods in Shallow Rivers. Water 13, 2808. https://doi.org/10.3390/w13202808.

Larnier, K., Monnier, J., Garambois, P.-A., Verley, J., 2021. River discharge and bathymetry estimation from SWOT altimetry measurements. Inverse Prob. Sci. Eng. 29, 759–789. https://doi.org/10.1080/17415977.2020.1803858.

Le Boursicaud, R., Pénard, L., Hauet, A., Thollet, F., Le Coz, J., 2016. Gauging extreme floods on YouTube: application of LSPIV to home movies for the post-event determination of stream discharges: application of LSPIV to Flood Home Movies. Hydrol. Process. 30, 90–105. https://doi.org/10.1002/hyp.10532.

Le Coz, J., Hauet, A., Pierrefeu, G., Dramais, G., Camenen, B., 2010. Performance of image-based velocimetry (LSPIV) applied to flash-flood discharge measurements in Mediterranean rivers. J. Hydrol. 394, 42–52. https://doi.org/10.1016/j.jhydrol.2010.05.049.

Le Coz, J., Camenen, B., Peyrard, X., Dramais, G., 2012. Uncertainty in open-channel discharges measured with the velocity–area method. Flow Meas. Instrum. 26, 18–29. https://doi.org/10.1016/j.flowmeasinst.2012.05.001.

Le Coz, J., Jodeau, M., Hauet, A., Marchand, B., Le Boursicaud, R., 2014. Image-based velocity and discharge measurements in field and laboratory river engineering studies using the free FUDAA-LSPIV software, in: Proceedings of the International Conference on Fluvial Hydraulics, River Flow. pp. 2014–05.

Lewis, Q.W., Lindroth, E.M., Rhoads, B.L., 2018. Integrating unmanned aerial systems and LSPIV for rapid, cost-effective stream gauging. J. Hydrol. 560, 230–246. https://doi.org/10.1016/j.jhydrol.2018.03.008.

Lewis, Q.W., Rhoads, B.L., 2018. LSPIV measurements of two-dimensional flow structure in streams using small unmanned aerial systems: 1. Accuracy assessment based on comparison with stationary camera platforms and in-stream velocity measurements. Water Resour. Res. 54, 8000–8018. https://doi.org/10.1029/2018WR022550.

Li, X., Zhang, B., Sander, P.V., Liao, J., 2019. In: Blind Geometric Distortion Correction on Images through Deep Learning. IEEE, Long Beach, CA, USA, pp. 4850–4859. https://doi.org/10.1109/CVPR.2019.00499.

Liu, W.-C., Lu, C.-H., Huang, W.-C., 2021. Large-Scale Particle Image Velocimetry to Measure Streamflow from Videos Recorded from Unmanned Aerial Vehicle and Fixed Imaging System. Remote Sens. (Basel) 13, 2661. https://doi.org/10.3390/rs13142661.

Lucas, B.D., Kanade, T., 1981. An iterative image registration technique with an application to stereo vision. Vancouver.

Meselhe, E.A., Peeva, T., Muste, M., 2004. Large scale particle image velocimetry for low velocity and shallow water flows. J. Hydraul. Eng. 130, 937–940. https://doi.org/10.1061/(ASCE)0733-9429(2004)130:9(937).

Mueller, D.S., Wagner, C.R., Rehmel, M.S., Oberg, K.A., Rainville, F., 2009. Measuring discharge with acoustic Doppler current profilers from a moving boat. US Department of the Interior, US Geological Survey Reston, Virginia (EUA).

Muste, M., Yu, K., Spasojevic, M., 2004. Practical aspects of ADCP data use for quantification of mean river flow characteristics; Part I: moving-vessel measurements. Flow Meas. Instrum. 15, 1–16. https://doi.org/10.1016/j.flowmeasinst.2003.09.001.

Muste, M., Fujita, I., Hauet, A., 2008. Large-scale particle image velocimetry for measurements in riverine environments: LARGE-SCALE PARTICLE VELOCIMETRY. Water Resour. Res. 44 https://doi.org/10.1029/2008WR006950.

Organization, W.M. (Ed.), 2008. Guide to Hydrological Practices, 6th, ed. ed. WMO. WMO, Geneva, Switzerland.

Patalano, A., García, C.M., Rodríguez, A., 2017. Rectification of image velocity results (RIVeR): a simple and user-friendly toolbox for large scale water surface particle image velocimetry (PIV) and particle tracking velocimetry (PTV). Comput. Geosci. 109, 323–330. https://doi.org/10.1016/j.cageo.2017.07.009.

Pavelsky, T.M., 2014. Using width-based rating curves from spatially discontinuous satellite imagery to monitor river discharge: SCIENTIFIC BRIEFING. Hydrol. Process. n/a–n/a.

Pearce, S., Ljubičić, R., Peña-Haro, S., Perks, M., Tauro, F., Pizarro, A., Dal Sasso, S., Strelnikova, D., Grimaldi, S., Maddock, I., Paulus, G., Plavšić, J., Prodanović, D., Manfreda, S., 2020. An Evaluation of Image Velocimetry Techniques under Low Flow Conditions and High Seeding Densities Using Unmanned Aerial Systems. Remote Sens. (Basel) 12, 232. https://doi.org/10.3390/rs12020232.

Perks, M.T., 2020. KLT-IV v1.0: image velocimetry software for use with fixed and mobile platforms. Geosci. Model Dev. 13, 6111–6130. https://doi.org/10.5194/gmd-13-6111-2020.

Perks, M.T., Dal Sasso, S.F., Hauet, A., Jamieson, E., Le Coz, J., Pearce, S., Peña-Haro, S., Pizarro, A., Strelnikova, D., Tauro, F., Bomhof, J., Grimaldi, S., Goulet, A., Hortobágyi, B., Jodeau, M., Käfer, S., Ljubičić, R., Maddock, I., Mayr, P., Paulus, G., Pénard, L., Sinclair, L., Manfreda, S., 2020. Towards harmonisation of image

velocimetry techniques for river surface velocity observations. Earth Syst. Sci. Data 12, 1545–1559. https://doi.org/10.5194/essd-12-1545-2020.

Pizarro, A., Dal Sasso, S.F., Manfreda, S., 2020a. Refining image-velocimetry performances for streamflow monitoring: Seeding metrics to errors minimization. Hydrol. Process. 34, 5167–5175. https://doi.org/10.1002/hyp.13919.

Pizarro, A., Dal Sasso, S.F., Perks, M.T., Manfreda, S., 2020b. Identifying the optimal spatial distribution of tracers for optical sensing of stream surface flow. Hydrol. Earth Syst. Sci. 24, 5173–5185. https://doi.org/10.5194/hess-24-5173-2020.

Pumo, D., Noto, L.V., 2023. Exploring the use of multi-gene genetic programming in regional models for the simulation of monthly river runoff series. Stoch Environ Res Risk Assess 37 (5), 1917–1941.

Pumo, D., Viola, F., La Loggia, G., Noto, L.V., 2014. Annual flow duration curves assessment in ephemeral small basins. J. Hydrol. 519, 258–270. https://doi.org/10.1016/j.jhydrol.2014.07.024.

Pumo, D., Alongi, F., Ciraolo, G., Noto, L., 2021. Optical methods for river monitoring: a simulation-based approach to explore optimal experimental setup for LSPIV. Water 13, 247. https://doi.org/10.3390/w13030247.

Pumo, D., Viola, F., Noto, L.V., 2013. ModABa Model: Annual Flow Duration Curves Assessment in Ephemeral Basins, in: EGU General Assembly Conference Abstracts. pp. EGU2013-8027.

Rahman Khan, M., Gourley, J.J., Duarte, J.A., Vergara, H., Wasielewski, D., Ayral, P.-A., Fulton, J.W., 2021. Uncertainty in remote sensing of streams using noncontact radars. J. Hydrol. 603, 126809 https://doi.org/10.1016/j.jhydrol.2021.126809.

Riggs, R.M., Allen, G.H., David, C.H., Lin, P., Pan, M., Yang, X., Gleason, C., 2022. RODEO: An algorithm and Google Earth Engine application for river discharge retrieval from Landsat. Environ. Model. Softw. 148, 105254 https://doi.org/10.1016/j.envsoft.2021.105254.

Shi, J., Tomasi, C., 1994. ᵃGood Features to Track, in: º Proc. IEEE Conf. Computer Vision and Pattern Recognition. pp. 593–600.

Tauro, F., Petroselli, A., Porfiri, M., Giandomenico, L., Bernardi, G., Mele, F., Spina, D., Grimaldi, S., 2016. A novel permanent gauge-cam station for surface-flow observations on the Tiber River. Geosci. Instrum. Method. Data Syst. 5, 241–251. https://doi.org/10.5194/gi-5-241-2016.

Tauro, F., Piscopia, R., Grimaldi, S., 2017. Streamflow Observations From Cameras: Large-Scale Particle Image Velocimetry or Particle Tracking Velocimetry? Water Resour. Philos. Phenomenol. Res. 53, 10374–10394. https://doi.org/10.1002/2017WR020848.

Thielicke, W., Stamhuis, E.J., 2014. PIVlab – towards user-friendly, affordable and accurate digital particle image velocimetry in MATLAB. Journal of Open Research Software 2. https://doi.org/10.5334/jors.bl.

Tomasi, C., Kanade, T., 1991. Detection and tracking of point. Int. J. Comput. Vis. 9, 137–154.

Watanabe, K., Fujita, I., Iguchi, M., Hasegawa, M., 2021. Improving accuracy and robustness of space-time image velocimetry (STIV) with deep learning. Water 13, 2079. https://doi.org/10.3390/w13152079.

Willmott, C.J., Robeson, S.M., Matsuura, K., 2012. A refined index of model performance. Int. J. Climatol. 32, 2088–2094. https://doi.org/10.1002/joc.2419.

Willmott, C.J., Wicks, D.E., 1980. An empirical method for the spatial interpolation of monthly precipitation within California. Phys. Geogr. 1, 59–73. https://doi.org/10.1080/02723646.1980.10642189.

Yeh, M.-T., Chung, Y.-N., Huang, Y.-X., Lai, C.-W., Juang, D.-J., 2019. Applying adaptive LS-PIV with dynamically adjusting detection region approach on the surface velocity measurement of river flow. Comput. Electr. Eng. 74, 466–482. https://doi.org/10.1016/j.compeleceng.2017.12.013.

Zhao, H., Chen, H., Liu, B., Liu, W., Xu, C.-Y., Guo, S., Wang, J., 2021. An improvement of the space-time image velocimetry combined with a new denoising method for estimating river discharge. Flow Meas. Instrum. 77, 101864 https://doi.org/10.1016/j.flowmeasinst.2020.101864.